

Original contains color plates. All DTIC reproductions will be in black and white.

REPOF

AD-A264 329

Form Approved
ORM No. 0704-0188

2

Public reporting burden for this collection of information is estimated to average 1 hour per response, including the time for reviewing instructions, searching existing data sources, gathering and maintaining the data needed, and completing and reviewing this collection of information, sending it to the Office of Management and Budget, Paperwork Project (0704-0188).



For reviewing instructions, searching existing data sources, gathering and maintaining the data needed, and completing and reviewing this collection of information, send it to the Office of Management and Budget, Paperwork Project (0704-0188), 15 Jefferson Davis Highway, Suite 1204, Arlington, VA 22202-4302, and to the Office of Management and Budget, Paperwork Project (0704-0188), Washington, DC 20503.

1. Agency Use Only (Leave blank)

1992

2. Report Type and Dates Covered.

Final Book Contribution

4. Title and Subtitle.

Chapter 7. Sea Ice Altimetry

5. Funding Number(s).

Program Element No. 0603604N

Project No. X1596

6. Author(s).

Florence M. Fetterer, Mark R. Drinkwater*, Kenneth C. Jezek**, Seymour W. C. Laxon***, Robert G. Onstott****, and Lars M. H. Ulander*****

Task No.

Accession No. DN251020

Work Unit No. 93212C

7. Performing Organization Name(s) and Address(es).

Naval Research Laboratory
Oceanography Division
Stennis Space Center, MS 39529-5004

DTIC
ELECTE
MAY 17 1993
S C D

8. Performing Organization

Report Number.

BC 004-92-321

9. Sponsoring/Monitoring Agency Name(s) and Address(es).

Space and Naval Warfare Systems Command
Washington, DC

10. Sponsoring/Monitoring Agency

Report Number.

BC 004-92-321

11. Supplementary Notes.

Published in Microwave Remote Sensing of Sea Ice. * California Institute of Technology, Pasadena, CA, ** The Ohio State University, Columbus, OH 43210, *** University College London, ****Environmental Research Institute of Michigan, Ann Arbor, MI, *****Chalmers University of Technology, Goteborg, Sweden

12a. Distribution/Availability Statement.

Approved for public release; distribution is unlimited.

12b. Distribution Code

13. Abstract (Maximum 200 words).

Using altimeter data for quantitative information about sea ice is an idea with relatively few proponents. Often the poor spatial sampling given by the altimeter's single-point measurements along widely spaced ground tracks and the difficulty of interpreting altimeter pulse echoes over ice are cited as reasons to avoid altimetry. It is becoming evident, however, that altimetry may be able to make unique measurements. For instance, the altimeter data record reveals the presence of small areas of open water within the pack at concentrations too low to be detected by a passive microwave sensor such as a Special Sensor Microwave/Imager (SSM/I) and too small to be resolved by satellite synthetic aperture radar (SAR).

98 5 14 006

93-10906



2490

14. Subject Terms

Remote sensing, synthetic aperture radar, altimeter, scatterometer

15. Number of Pages.

25

16. Price Code.

17. Security Classification of Report.

Unclassified

18. Security Classification of This Page.

Unclassified

19. Security Classification of Abstract.

Unclassified

20. Limitation of Abstract.

SAR

Chapter 7. Sea Ice Altimetry

FLORENCE M. FETTERER

Remote Sensing Branch, Naval Research Laboratories, Stennis Space Center, Mississippi 39529-5004

MARK R. DRINKWATER

Jet Propulsion Laboratory, California Institute of Technology, 4800 Oak Grove Drive, Pasadena, California 91109

KENNETH C. JEZEK

Byrd Polar Research Center, 1090 Carmack Road, The Ohio State University, Columbus, Ohio 43210

SEYMOUR W. C. LAXON

University College London, Mullard Space Science Laboratory, Holmbury St. Mary Dorking, Surrey, RH5 6NT, United Kingdom

ROBERT G. ONSTOTT

Environmental Research Institute of Michigan, P. O. Box 8618, Ann Arbor, Michigan 48107

LARS M. H. ULANDER

Department of Radio and Space Sciences, Chalmers University of Technology, S-41296 Goteborg, Sweden

7.1 INTRODUCTION

Using altimeter data for quantitative information about sea ice is an idea with relatively few proponents. Often the poor spatial sampling given by the altimeter's single-point measurements along widely spaced ground tracks and the difficulty of interpreting altimeter pulse echoes over ice are cited as reasons to avoid altimetry. It is becoming evident, however, that altimetry may be able to make unique measurements. For instance, the altimeter data record reveals the presence of small areas of open water within the pack at concentrations too low to be detected by a passive microwave sensor such as a Special Sensor Microwave/Imager (SSM/I) and too small to be resolved by satellite synthetic aperture radar (SAR).

At high latitudes the net laid down by a satellite altimeter's ground track becomes dense, and spatial sampling (over a period of days) can approach the resolution of SSM/I. A satellite altimeter's along-track resolution of less than a kilometer is better than that of SSM/I, and the altimeter's sensitivity in detecting the ice edge is greater. The low data rate makes it possible to process altimetry in near-real time. For these reasons, an ice edge product derived from Geosat altimeter data has been used operationally at the Navy/National Oceanic and Atmospheric Administration (NOAA) Joint Ice Center to supplement infrared imagery for estimating ice edge position [Hawkins and Lybanon, 1989].

Microwave Remote Sensing of Sea Ice
Geophysical Monograph 68
©1992 American Geophysical Union

Objections concerning the difficulty of interpreting altimetry over ice are more difficult to meet, in part because of the paucity of ground truth or imagery coincident with altimetry. In this chapter, we cover some of the research into understanding altimeter backscatter over sea ice and interpreting altimeter data in terms of parameters such as ice type, concentration, edge location, and wave penetration in the marginal ice zone.

7.2 INSTRUMENT DESCRIPTION

7.2.1 Instrument Design

Satellite altimeters have evolved steadily from Skylab, which in 1973 demonstrated the concept of altimetry from space. Development continued through GEOS-3 in 1975 until the 1978 launch of Seasat, which carried the first altimeter capable of measuring sea surface topography with an error of only a few centimeters. Precision in range or height measurement is obtained through a design that takes advantage of the ocean's near-Gaussian wave height distribution and uniform dielectric characteristics. Over ice, where surface height distributions and dielectric characteristics vary sharply from place to place, measurements of height and backscatter are often misleading. Therefore, it is necessary to understand how altimeters are designed to operate before one interprets altimeter backscatter from sea ice. Altimeters planned for the 1990's will refine rather than change the Seasat design, upon which the following description is based. Hereafter, similar altimeters such as Geosat and ERS-1 will be called ERS-1 class altimeters.

ACCEPTED	✓
NTIS GRA&I	
DTIC TAB	
Unannounced	
Justification	
By	
Distribution /	
Availability Cod	
Avail and/or Spec	
A-1	20

7.2.2 Pulse Limited Altimetry

Satellite altimeters use pulse width-limited geometry. A wide-beam (with a 3-dB half-width of 0.8° for Seasat), relatively long (on the order of microseconds) pulse is emitted, and the pulse echo is processed in a way equivalent to measuring the travel time to the surface and back of a much shorter pulse only a few nanoseconds long. This technique of pulse compression gives high range resolution. (For a full explanation of pulse compression on satellite altimeters, see Chelton et al. [1989]). The area on the surface illuminated by the pulse grows with time until the trailing edge of the pulse leaves the lowest reflecting points at nadir (Figure 7-1). The maximum area simultaneously illuminated, then, depends on the surface height distribution and effective (compressed) pulse length. This area is usually referred to as the pulse-limited footprint (PLF). For Seasat, the diameter of the PLF was 1.6 km for a smooth sea and grew to 7.7 km for a significant wave height (SWH) of 10 m. As the pulse continues to move out over the surface, the footprint becomes an annulus of constant area and increasing circumference. It is important to note that due to irregularities in surface roughness and slope, the true illuminated area at any time may be irregular in shape or discontinuous. Over ridged sea ice, for instance, an off-nadir ridge sail may be high enough to be illuminated at the same time as the ice near nadir.

Altimeters that use beam width-limited geometry emit a narrow beam and do not rely on pulse-compression techniques for accurate range measurements. Footprint size depends only on beam width and satellite altitude. This geometry is not used for satellite altimeters because precise antenna pointing capability is a necessity and the antenna size and gain required to generate a narrow beam are large. However, use of a beam width-limited altimeter would simplify interpretation of signals over ice, because footprint area remains constant regardless of the surface height distribution [Rapley et al., 1983].

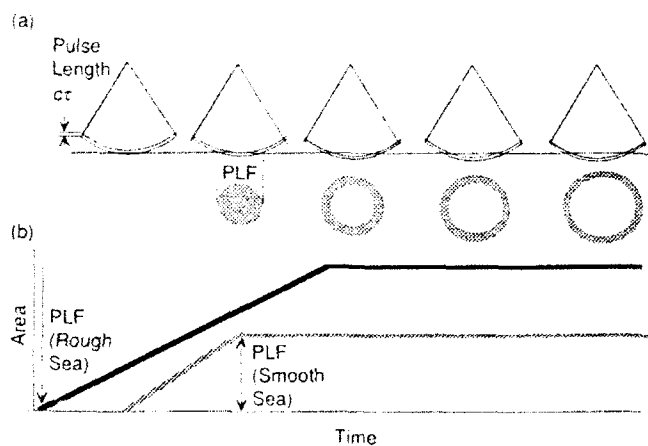


Fig. 7-1. (a) Area illuminated by a pulse hitting the smooth ocean's surface and (b) the growth of the footprint area with time for smooth and rough seas. The PLF is larger for meter-scale roughness, since the time required for the pulse to travel from crest to trough exceeds the effective pulse length. Graph is not to scale.

On board the satellite, the echo of the emitted pulse is differenced with a deramping signal. The frequency of the emitted pulse changes over the pulse length in a linear chirp or ramp. The total change in frequency over the ramp is the bandwidth of the instrument. The deramping signal (so-called because the effect of this processing step is to remove the ramp in frequency from the pulse echo) is generated at a delay time t_0 , determined by the onboard tracking unit. This time corresponds to the expected arrival time at the receiver of the reflected pulse from mean sea level. The resulting signal is a mixture of returns from individual point scatterers. Echoes from wave crests arrive first and are therefore shifted earlier in time from tracking time t_0 . For a pulse-limited altimeter, returns shifted later than t_0 come not only from points below mean sea level, but also, as the footprint expands, from scatterers distant from nadir. If the height distribution for the area over which the pulse expands remains Gaussian throughout, the shape of the signal $S(t)$ resulting from all scatterers is given by the convolution of functions describing the transmitted pulse shape, the antenna gain pattern, and the surface height distribution [Drinkwater, 1991]. This signal is the pulse echo waveform (Figure 7-2). The half-power point is at delay time t_0 , which gives the range to mean sea level. Maximum power occurs at the delay time at which the maximum footprint area is achieved. At later delay times, power drops off due to the antenna gain pattern. Over the ocean, the slope of the leading edge (or ramp) of the waveform is inversely proportional to SWH, and the peak power is related to wind speed. The characteristic shape of this signal only holds for reflecting surfaces of meter-scale roughness for which specular point scattering can be assumed.

The digitally sampled waveform has a value at 60 (for Seasat) contiguous time intervals, centered, if the tracker is operating correctly, on the half-power point. The time intervals, or range gates, each correspond to a two-way travel time resolution of 3.125 nanoseconds, which is equivalent to a range resolution of about 1 meter. (Better precision in the range to nadir or height measurement is obtained through averaging). The power in the range gates

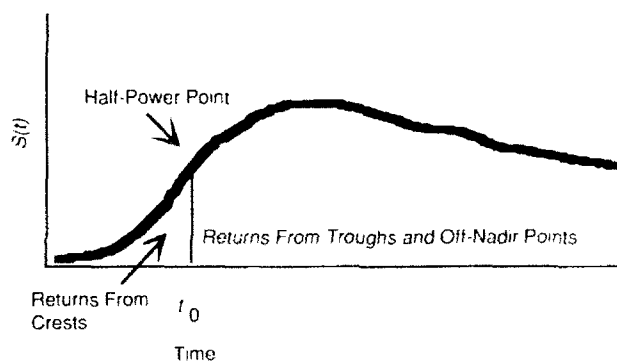


Fig. 7-2. The pulse echo for pulse-limited altimetry and a Gaussian surface height distribution. The half-power point at t_0 corresponds to the delay of returns from the mean sea level.

is the result of backscatter from range rings within the altimeter footprint (Figure 7-3). The area covered by each range ring is equal to that of the PLF

$$A_{\text{plf}} = \pi r_{\text{plf}}^2 \approx \pi c H \tau \quad (1)$$

where r_{plf} is the radius of the PLF, H is satellite height above the surface, and τ is compressed pulse length (neglecting, for simplicity, the Earth's curvature). With this expression for area, it is possible to use the radar equation to arrive at an expression for the power received from any range ring

$$P_{\text{range ring}} = P_t \frac{G^2 \lambda^2 L_{\text{atm}} c \tau}{4(4\pi)^2 H^3} \sigma \quad (2)$$

where L_{atm} is atmospheric attenuation loss. Using a form of this equation, backscatter can be retrieved from waveform range gate samples. For Geosat, the formula is

$$\sigma_i^0 = 10 \log_{10} P_i + AGC + K + 30 \log_{10} \frac{H}{H_0} + L_{\text{atm}} \quad (3)$$

where P_i is the power in range ring i expressed in counts, H_0 is a reference height, AGC is the attenuator setting (de-

scribed in Section 7.2.4), and K is a constant dependent on system parameters [Ulander, 1987a]. The peak backscatter usually appears in one of the first few range rings for sea ice and is generally assumed to be the backscatter from nadir. When altimeter backscatter measurements are referred to in what follows, it is usually the peak backscatter that is meant.

While the PLF corresponds to that part of the waveform over which the maximum power is reached, the range window-limited footprint corresponds to the area mapped out by the pulse at the end of the time corresponding to the last range gate. For Seasat, the diameter of the range window-limited footprint was about 10 km, and the angle of incidence at the last range ring was about 0.3° .

7.2.3 Waveform Averaging

In the case of noncoherent scattering, the phase relationships of returns from all facets or specular points are random. The vector sum of amplitude and phase for reflections within a range ring is different for each range ring, which lends noise or fading characteristics to individual pulse echoes. Therefore, waveforms are averaged to reduce fluctuations and to provide a good estimate of height (given by the half-power point) and backscatter. Each waveform must be a statistically independent sample. The pulse repetition frequency (PRF) necessary to avoid correlation between pulse echoes depends on the surface roughness and orbital velocity. Seasat used a PRF of 1020 Hz. Fifty echoes were averaged, during which time the satellite nadir track moved about 330 m. For altimetry over the ocean, averaging 50 echoes is a good compromise that provides enough samples for an accurate power estimate while not degrading the along-track spatial resolution of the measurement beyond acceptable bounds, given the typical scale of changes in dynamic sea surface height, wind speed, and SWH. When surface characteristics are changing over the integration time (as is often the case over ice), or when pulse echoes are dominated by one or several strong scatterers, waveforms that result from averaging will not truly represent the surface.

7.2.4 The Adaptive Tracker and Processing Loops

Accurate estimates of height and other parameters derived from waveforms depend on accurate superposition of pulse echoes for averaging. This, in turn, depends on proper timing of the deramping pulse. The following description of the method by which this is achieved is based on the Seasat adaptive tracking unit, but Geosat and ERS-1 trackers are similar in concept. The adaptive tracker tracks waveforms through an automatic gain control (AGC) loop and tracking (or range and range rate) loops. The AGC component of the tracking system constantly adjusts the gain of the receiver to achieve the maximum signal-to-noise ratio. Power within the (averaged) waveform is computed according to

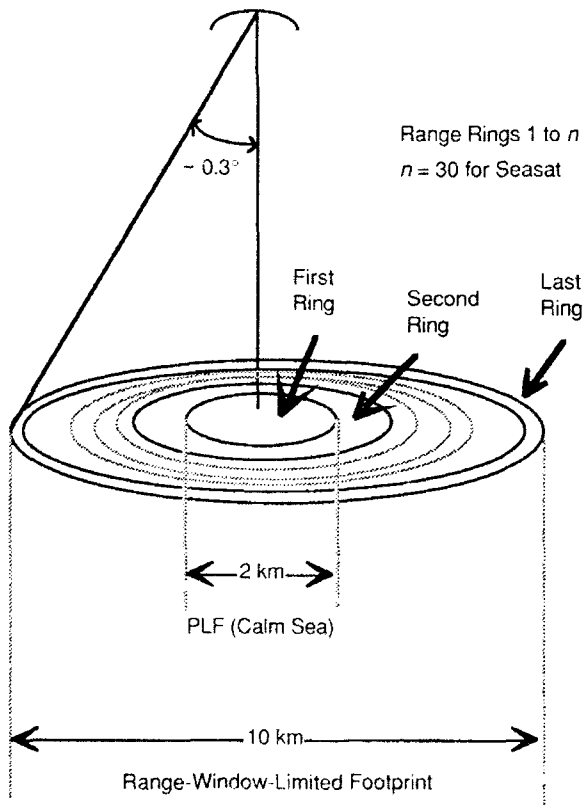


Fig. 7-3. Altimeter footprint range rings (not to scale). Each ring corresponds to a range gate in the digitally sampled waveform.

$$AGC_{gate} = Sc \sum_{i=1}^{60} P_i \quad (4)$$

where i is range gate number, P is the power (expressed as a count value) in each gate, and Sc is a scale factor, Figure 7-4(a). An attenuation value is computed according to the recursion relation

$$AGC(n+1) = AGC(n) + a\Delta AGC \quad (5)$$

where ΔAGC is the difference between AGC_{gate} and some reference, and a is some constant (0.0265 for Seasat). The AGC loop works to keep the average power in the waveform constant. It is updated at a rate of 20 Hz (every 50 pulses), and the new value is applied to the next 50 pulse echoes. Because of the factor a in the recursion relation, an adjustment to the value of AGC necessitated by a change in backscatter from the surface takes place over 0.8 seconds, during which time the satellite moves 5.3 km. While the parameter AGC is a good estimator of backscatter over the ocean, this is not the case over ice, where peak power can change an order of magnitude in a much shorter distance. Therefore, to retrieve high-frequency variability in backscatter it is necessary to take into account the count values in each waveform, along with the AGC value that was the attenuator setting during the waveform integration time. In such cases where backscatter is changing quickly, AGC

is overestimating or underestimating power, and the signal-to-noise ratio will not be optimal.

In Figure 7-4 (typical of ocean signals), the value of AGC_{gate} is about equal to half the power in the waveform. The power in the center of the range window is measured in a middle gate M , which is sometimes called gate 30.5, Figure 7-4(b). The tracker seeks to minimize the range error Δr , where

$$\Delta r = AGC_{gate} - M_{gate} \quad (6)$$

by shifting the range window (in time) to keep the half-power point in M . The width of gate M depends on the slope of the leading edge of the waveform, and therefore on SWH. The tracker adapts the width of M in range gates based on the difference between power in an early gate E at the bottom of the ramp and a later gate L at the top of the ramp. For a significant wave height of less than 2 m, gate M is a single range gate wide (Chelton et al., 1989).

The range error Δr is used to predict the range to the surface (and therefore the delay time t_d at the center of the range window) for subsequent pulses according to

$$r(n+1) = r(n-1) + a\Delta r(n) + b(n-M) \quad (7)$$

where Δr is the range error for pulse n , a is the tracker time constant, M is the update interval of the loop, and

$$\dot{r}(n) = \dot{r}(n-1) + b \frac{\Delta r(n)}{\Delta t} \quad (8)$$

is the range rate. Time constants a and b can be adjusted to increase the agility of the tracker (at the price of increased noise). Different designs for tracking ocean and nonocean surfaces have been explored [McIntyre et al., 1986; Rapley et al., 1983; Ulander, 1987c]. The ERS-1 altimeter has both an ocean mode, which uses a Suboptimal Maximum Likelihood Estimator (SMLE) tracker, and an ice mode, which has a split-gate tracker unlike the Seasat-Geosat tracker [Griffiths et al., 1987]. The ice mode tracker has a wider range window for better tracking over undulating continental ice shelves. For sea ice, however, it is not height variations confounding the agility of the tracker, but rather backscatter variations within the footprint, which introduce errors exacerbated by interaction between the processing loops.

7.2.5 Errors Common Over Ice

Figure 7-5 illustrates how the rapid rise and fall of sea ice waveforms confounds the tracker selection of gates E , M , and L . Because of the steepness of the ramp and the rapid fall-off from the peak value in the return waveform in Figure 7-5(a), the power in M is not half the average power

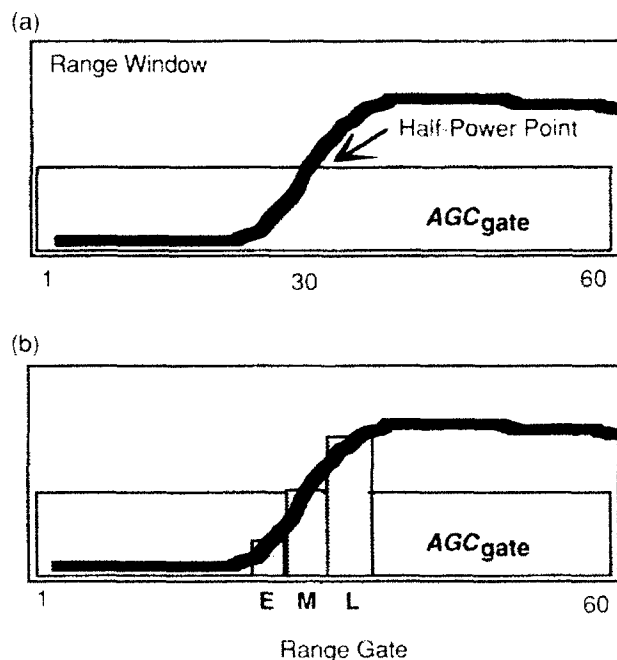


Fig. 7-4. The altimeter range window and gates. (a) Over the ocean, the power in AGC_{gate} should equal half the power in the waveform. The half-power point occurs at time t_0 if the tracker is operating correctly. (b) Early (E), middle (M), and late (L) gates in the center of the waveform determine the slope of the ramp (proportional to SWH). The half-power point should be in gate M.

in the waveform. Power within the AGC gate is much less than that within the middle gate. In extreme cases, this results in a large negative height error, causing the tracker to shift the range window so that subsequent pulses appear later in the range window, Figure 7-5(b). On the next update cycle, the middle gate measures the noise before the ramp, resulting in a large positive height error. The tracker corrects for this until the peak is in the middle gate again when the error repeats. This error, called tracker oscillation, is evident in data that exhibits height excursions. Tracker oscillation can sometimes be corrected by retracking the waveforms. Retracking involves (1) applying an algorithm to the waveform record that finds the point on the waveform that should correspond to return from the surface at nadir, and (2) using the position of that point relative to the center of the range window to correct the height estimate based on the range window.

The range and range rate loops, like the AGC loop, were updated at 20 Hz (every 50 pulses) on Geosat and Seasat. Pulse echoes acquired with the same loop settings were averaged to make waveforms. However, waveforms were telemetered at 10 Hz, so the telemetered waveform is the average of two 50-pulse mean waveforms from two tracking loop updates. If the position of the range window is changing rapidly (due to changing topography or tracker oscillation), the resulting telemetered waveform will be a blurred or sometimes double-peaked composite, Figure 7-6(a). Errors resulting from the incorrect superposition of waveforms for averaging are termed telemetry summing errors [Rapley et al., 1987]. ERS-1 telemeters waveforms at the tracker loop update rate (20 Hz), thereby avoiding the problem that appeared in Seasat and Geosat data.

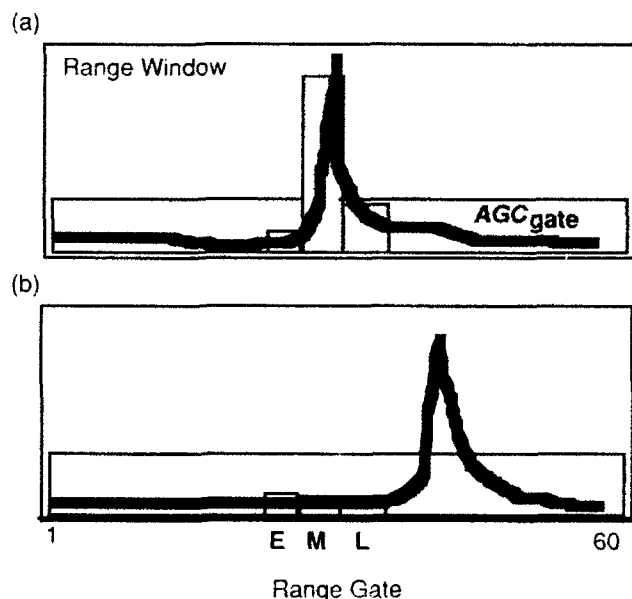


Fig. 7-5. (a) The ramp of a typically peaked waveform from sea ice can appear entirely in gate M. (b) This causes the tracker to shift the range window earlier in time for the next update cycle.

Tracker oscillation cannot be completely eliminated by retracking if telemetry summing errors are present, Figure 7-6(b). However, the probability that such errors exist can be estimated by examining the range rate parameter, which will peak when the range window is changing at the greatest rate and the probability of blurring is highest [Laxon, 1989]. The combined effect of tracker oscillation and telemetry summing, when it produces a sudden shift in range and blurred or double-peaked waveforms, is sometimes referred to as height glitch.

When the AGC loop sets the AGC value too low to accommodate power in the peaked portion of an ice waveform, saturation occurs. Saturation was common in Seasat data [Wingham and Rapley, 1987]. It is often associated with frequency splatter, Figure 7-6(c), where power from the saturated gate appears in earlier and later gates. Another artifact often present in ice data is snagging or "off-ranging." This occurs when a bright feature at nadir is followed by the tracker as it recedes, until it is sufficiently far from nadir for the true nadir return to once again dominate. Often this occurs at a transition from pack to fast ice, or from thin ice to multiyear (MY) ice [Laxon, 1989].

Antenna off-pointing was a serious problem with Geosat. Occasionally, the off-pointing was severe enough to cause loss of lock, a situation where the waveform disappears from the range window entirely for a few telemetry frames.

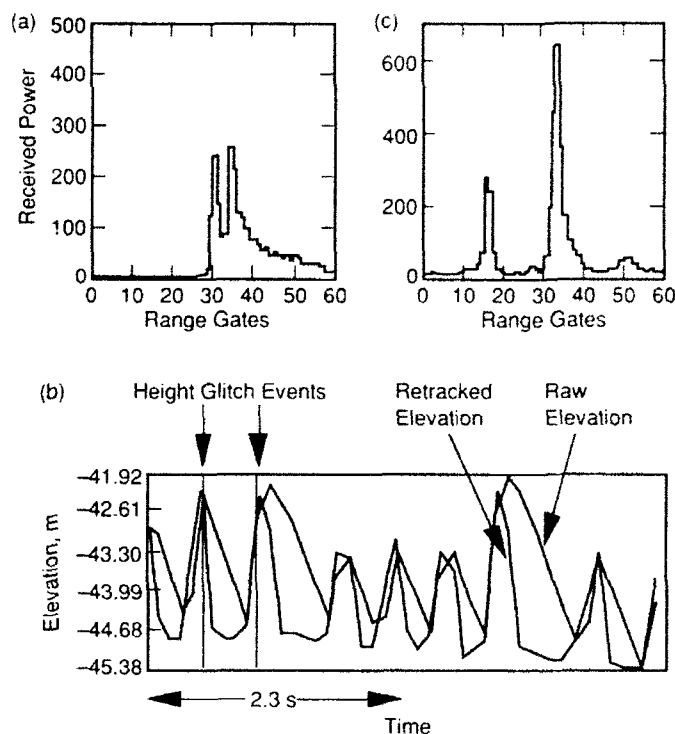


Fig. 7-6. Common errors in altimetry over sea ice. (a) An example of telemetry summing causing double peaking in a Seasat waveform over ice [Ulander, 1987b]. (b) Seasat data showing oscillation in the onboard height measurement. Retracking does not remove the oscillation due to telemetry summing errors [Laxon, 1989]. (c) A saturated Seasat waveform [Ulander, 1987b].

Over the ocean, off-pointing can be identified by the attendant rise in power in later gates, and a correction can be applied. Over sea ice, unpredictable waveform shapes make this impossible, resulting in altered waveform shapes and unidentifiable errors in height and backscatter measurements. The stabilizer used on ERS-1 should prevent off-pointing from being a serious problem.

Once the altimeter record over ice has been retracked and edited, the backscatter coefficient for any range gate can be found from the waveform using Equation (3) with the telemetered waveform range gate count values and the value of the attenuator setting (AGC). However, it is important to remember that the altimeter moves about 0.66 km between telemetered waveforms (for Geosat and Seasat). If the statistics of the surface are not stationary over that distance, the backscatter estimates may be misleading.

7.3 SEA ICE SCATTERING MODELS AT NORMAL INCIDENCE

7.3.1 Introduction to Altimeter Backscatter Models

The distinguishing characteristics of ice waveforms are that they are often narrow-peaked in shape, taper off quickly with incidence angle, have high backscatter coefficients at nadir, and are widely variable. Average annual values of Seasat backscatter over Arctic and Antarctic sea ice ranged from approximately 0 to 45 dB, with a mean greater than 20 dB [Laxon, 1989]. In contrast, backscatter over the ocean has a range of between 8 and 15 dB, depending on sea state [Chelton and McCabe, 1985]. On the basis of dielectric characteristics alone, one would expect ocean backscatter to be greater than that for ice, and indeed for surface measurements of backscatter at nadir this is usually the case. The dynamic range of altimeter measurements over ice cannot be explained by variability in the dielectric characteristics of ice alone. Since backscatter for airborne and satellite altimeters is dominated by surface rather than volume scattering, the nature of altimeter pulse echoes must be primarily determined by surface roughness. Specular or coherent reflection from smooth surfaces near nadir may produce the peaked component of waveforms, while diffuse reflection from rough surfaces may account for power in later, off-nadir gates. But while sea ice or ocean surfaces can in certain circumstances be extremely smooth, the question remains as to whether these surfaces are smooth over large enough areas to contribute coherent returns. Models that invoke only noncoherent (diffuse) reflection, on the other hand, may have difficulty describing the high backscatter from nadir and narrow peaked shape often seen over ice.

The physical characteristics of sea ice are quite variable, which compounds the modeling problem. Sea ice consists of both level and deformed ice of different ages, often with superimposed dry or wet snow layers. Water openings of different sizes and with variable wind conditions are often present. The different layers and interfaces of the snow, ice, and water may all contribute to the scattering of electro-

magnetic waves. Depending on the frequency used, however, it is often possible to neglect particular scattering terms and thus simplify the scattering computation. For example, the surface will appear rough and result in the dominance of diffuse scattering if the surface height variations are large compared with the radar wavelength. The dependence of surface roughness upon radar wavelength is expressed in parameters $k\sigma$ and kl , where $k = 2\pi/\lambda$, σ is the standard deviation of surface height, and l is the correlation length of surface roughness. These parameters determine the range of validity for commonly used models. In the following, we consider surface scattering close to normal incidence. The emphasis is on radar wavelengths in the Ku-band (1.7 to 2.4 cm), since most radar altimeters used for geophysical remote sensing operate in this band.

7.3.2 Backscatter From a Stationary Gaussian Random Surface

This section concerns backscatter from level and snow-free sea ice. The ice is modeled as a homogeneous medium with constant dielectric constant. Its surface has small-scale height variations represented by a stationary Gaussian process. The electromagnetic scattering from such a surface has been studied extensively in the past, but a general closed-form solution has not yet been found. A recently developed model for a perfectly conducting [Fung and Pan, 1987] and dielectric [Chen and Fung, 1991] surface has promise, but its range of validity has not yet been determined. High- and low-frequency solutions, however, are readily available and are sufficient for the present discussion.

7.3.2.1. Specular backscatter from a perfectly smooth surface. A surface is usually considered smooth if it meets the Rayleigh criterion. For Ku-band, σ must be less than about 0.3 cm. The scattering pattern for such a surface will show a large phase-coherent component of backscatter in the specular (nadir) direction and a much smaller diffuse component at other incidence angles. If a surface is perfectly smooth and planar, scattering is confined to the specular direction, with no diffuse component, and is equivalent to ray reflection. Such a surface will produce true specular reflection if it is perfectly smooth over at least two Fresnel zones. The edge of each circular Fresnel zone is defined where the phase of the reflected wave has changed by 0.5π compared with a reflection from the nadir point. The diameter of the first zone is given by

$$D_F = (2\lambda H)^{1/2} \quad (9)$$

or about 180 m for an ERS-1 class altimeter. Although possible in theory, it is unlikely that the rms height of the surface is perfectly smooth, or even smooth to within a few millimeters, over an area of several hundred square meters.

It is not convenient to describe true specular reflection in terms of a backscatter coefficient. However, it is possible to derive an effective backscatter coefficient that is dependent

on the radar system. For example, the backscatter coefficient of an infinitely large dielectric mirror observed by a pulse-limited altimeter is given by [Ulander, 1987a]

$$\sigma_{\text{coh}}^0 = |R(0)|^2 \frac{H}{c\tau} \quad (10)$$

where $R(0)$ is the Fresnel reflection coefficient $R(\theta)$ evaluated at 0° . The subscript indicates that reflection is, of course, coherent. The theoretical maximum return for an ERS-1 class altimeter, then, is about 48 dB, assuming an ice reflection coefficient of about -11 dB.

7.3.2.2. Coherent backscatter from a slightly rough planar surface. When a small rms surface roughness is superimposed on a flat, planar reflecting surface, an expression may be derived for the coherent backscattering coefficient, σ_{coh}^0 , which accounts for the sphericity of the wavefront and the radar system impulse response [Fung and Eom, 1983]:

$$\sigma_{\text{coh}}^0 = \frac{|R(\theta)|^2}{\beta_{\text{plf}}^2} \exp \left[-4k^2 \sigma^2 + \frac{\theta^2}{\beta_{\text{plf}}^2} \right] \quad (11)$$

Equation (11) assumes a Gaussian beam described by the one-sided pulse-limited beam width β_{plf}^2 , where $\beta_{\text{plf}} = c\tau/H$. At normal incidence this simplifies to [Ulander and Carlström, 1991]:

$$\sigma_{\text{coh}}^0 = |R(0)|^2 \frac{H}{c\tau} \exp(-4k^2 \sigma^2) \quad (12)$$

Figure 7-7 illustrates the coherent backscatter function derived using Equation (11) with suitable parameters for the ERS-1 altimeter and the Rutherford Appleton Laboratory (RAL) airborne altimeter [Drinkwater, 1987] respectively. For the satellite case, the fall-off in σ_{coh}^0 is extremely rapid for all surface roughnesses. The maximum backscatter values of between 40 and 48 dB occur for slightly rough surfaces typifying new saline ice (i.e., $\epsilon^* = 4.0 + j0.4$). In contrast, the RAL altimeter, with a pulse-limited beam width of 0.63° , gives a much wider response function that is lower in peak power at all roughnesses. These results demonstrate the role that the compressed pulse length and altitude of the altimeter play in dictating the coherent response function of a slightly rough surface. In short, the system impulse response is the most important factor in determining the decay of the coherent scattering coefficient with incidence angle. Furthermore, the coherent power is sharply reduced as the surface roughness increases only slightly.

7.3.2.3. Noncoherent backscatter from a rough surface where kl is large, but $k\sigma$ is small. Field measurements of sea ice surface roughness typically show that the rms height σ

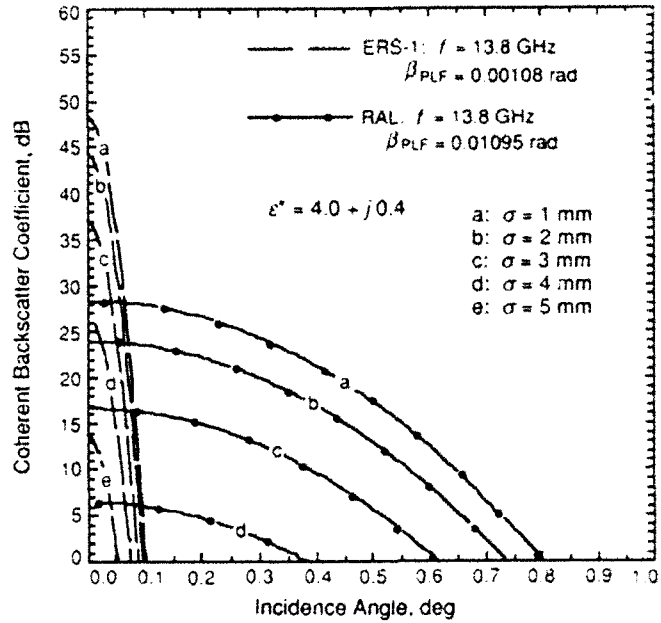


Fig. 7-7. Coherent backscatter versus incidence angle for space and airborne platforms.

is 0.1 to 1.0 cm and the height correlation function is exponential or Gaussian with a correlation length l of 2 to 10 cm [Ulander, 1991]. For radar wavelengths in the Ku-band, this ice surface is in the intermediate roughness range. Note that the correlation length is generally larger than the radar wavelength. The Kirchhoff approximation can therefore be used to evaluate the scattering integrals [Beckmann and Spizzichino, 1963]. This approach uses the diffraction integral for the scattered field and the tangent-plane approximation to compute the surface currents. The latter requires that the average radius of curvature of scattering elements be large compared to the wavelength. The rms surface slope must also be less than 0.25 radians in order to allow computation of an approximate (scalar) solution for dielectric surfaces. With these restrictions, the noncoherent backscatter coefficient σ_{non}^0 is given by [Ulaby et al., 1982]

$$\sigma_{\text{non}}^0(\theta) = |R(\theta)|^2 2k^2 \cos^2 \theta \exp(-g) \sum_{n=1}^{\infty} \frac{g^n}{n!} W^n(2k \sin \theta, 0) \quad (13)$$

where $g = (2k\sigma \cos \theta)^2$ and the first-order slope term that is important for larger incidence angles has been excluded. In Equation (13), the roughness spectrum $W^n(K_x, K_y)$ is related to the n^{th} power of the correlation function defined by [Fung and Pan, 1987]

$$W^n(K_x, K_y) = \frac{1}{2\pi} \int_{-\infty}^{\infty} \int_{-\infty}^{\infty} \rho^n(\xi, \zeta) \exp(-jK_x \xi - jK_y \zeta) d\xi d\zeta \quad (14)$$

where $\rho(\xi, \zeta)$ is the two-dimensional normalized height autocorrelation function. Analytical expressions for the

integral in Equation (14), when the surface is isotropic and has a Gaussian or exponential correlation function, can be found in Ulaby et al. [1982] and Kim et al. [1985], respectively.

7.3.2.4. Noncoherent backscatter from a rough surface where kl and $k\sigma$ are large. In the Kirchhoff or physical optics theory, when rms height is much larger than the radar wavelength it is possible to evaluate the diffraction integral using a stationary phase approximation [Beckmann and Spizzichino, 1963]. This corresponds to the geometric optics limit, in which the surface is assumed to be made up of tangent planes or specular facets that are infinitely large with respect to a wavelength. Thus it is often known as specular point theory. For such rough surfaces, backscatter is completely noncoherent and the backscatter coefficient is given by [Ulaby et al., 1982]

$$\sigma(\theta) = \frac{R(0)^2}{s^2 \cos^4 \theta} \exp\left(-\frac{\tan^2 \theta}{s^2}\right) \quad (15)$$

where s^2 is rms slope in radians.

The scalar and tangent-plane approximations, Equations (13) and (15), respectively, both give the mean noncoherent backscatter from a stationary Gaussian random surface. Since backscatter is being summed noncoherently, if an altimeter were to scan such a rough surface the returned power would exhibit statistical fluctuations or signal fading (described in Section 7.2.3). The return power is then distributed according to a negative-exponential or Rayleigh distribution, provided that the following conditions are satisfied:

- (1) Many individual scattering elements contribute to the returned power, and no single one dominates.
- (2) The amplitude and phase of returns from the scatterers are independent, and the phase distribution is uniform.

7.3.3 Backscatter From a Heterogeneous Random Surface

Equations (11) and (12) show that the coherent return is a highly nonlinear function of the rms surface height. When the rms height changes only from 0.2 to 0.4 cm, the coherent component is reduced by 17 dB. This suggests that the normal-incidence response is dominated by the smoother parts of the surface for which the rms height is a tenth of a wavelength or less. The first model to recognize this fact was that proposed by Brown [1982]. The model assumes that the scattering originates from an ensemble of circular, horizontal, and flat dielectric patches near nadir. The patches are assumed to cover a small fraction of the surface, to be located at the same height, and to be randomly distributed in the horizontal plane. Brown shows that both a coherent and a noncoherent component result from this model. The former is caused by the patches being located at the same vertical level, to within a few mm, and is propor-

tional to the number of patches squared. The latter is caused by the random horizontal distribution of the patches and is directly proportional to the number of patches. Although the model recognizes the importance of the spatial variability of the surface characteristics, it inherently assumes that reflections from the patches add coherently. This assumption is probably unrealistic in practice, at least for spaceborne systems, due to the large first Fresnel zone.

Another model has been proposed which does not require the flat patches to add coherently [Ulander and Carlstrom, 1991]. The backscattered power is instead assumed to be dominated by reflections from horizontal and flat patches that add noncoherently. A narrow-peaked waveform may occur if the patches are sufficiently large. This assumption is more realistic, but field measurements are presently lacking to verify it. Using physical optics, the radar cross section from a single circular and flat dielectric patch is given by

$$\sigma(\theta) = A R(0)^2 \left(\frac{\pi D}{\lambda}\right)^2 \exp\left(-\frac{\theta^2}{\theta_D^2}\right) \quad (16)$$

where A is the patch area, D is the patch diameter, and the angular response has been approximated by a Gaussian function with $\theta_D \approx 0.3 \lambda/D$. For a collection of sparsely distributed and horizontal patches, we then obtain the backscattering coefficient according to

$$\sigma^0(\theta) = F \frac{\sigma(\theta)}{A} = A R(0)^2 \left(\frac{\pi D}{\lambda}\right)^2 \exp\left(-\frac{\theta^2}{\theta_D^2}\right) \quad (17)$$

where F is the fractional coverage of flat patches.

Equation (17) does not take the altimeter system impulse response into account. When the patch diameter is sufficiently large to produce a narrow-peaked waveform, the effective backscattering coefficient is given by

$$\sigma^0 \approx \frac{1}{\tau} \int_0^\infty \sigma^0\left(\frac{c\tau}{H}\right)^2 d\tau = 0.9 F R(0)^2 \frac{H}{c\tau} \quad (18)$$

Typical values for the narrow-peaked backscatter coefficient, as measured by spaceborne altimeters, are 20 to 40 dB, corresponding to $F \approx 0.2\%$ to 16% according to Equation (18). In this class of surface, the coherent component can exhibit signal fading as the number of patches or reflecting facets within the first Fresnel zone varies from pulse to pulse. Although the terms *specular* and *coherent* reflection are often used interchangeably, true specular reflection originates from a single infinitely large (when compared with the PLF) mirror-like facet and does not show fluctuations in amplitude and phase from pulse to pulse.

It is also possible to modify the Kirchhoff models according to Equations (13) and (15) to include the effects of a heterogeneous surface and to produce a narrow-peaked waveform. We here give the result for the geometric-optics model

$$\sigma^0 = \frac{1}{\tau} \int_0^\infty \sigma^0 \left(\frac{c\tau}{H} \right)^{1/2} d\tau \approx FR |\rho|^2 \frac{H}{c\tau} \quad (19)$$

which only differs by a factor 0.9 from Equation (18). This shows that the geometrical optics and flat patch model predictions are indeed very similar, although the scattering mechanisms assumed are very different. The approach taken by Ulander and Carlström [1991] is more realistic in that it accounts for height distributions or surface tilting of patches and is not restricted by the approximation of scattering by individual facets to the scattering from smooth specular points. But while the assumptions of the other models are simplistic, the notion that scattering from many individual surface elements conforms reasonably closely to that from a specular surface appears not too far from the truth.

7.3.4 Discussion

In order to contrast normal incidence coherent and noncoherent components of a waveform, we consider here the relative difference in their power using an expression for the ratio of noncoherent to coherent backscatter. The expression is dependent upon the radar system parameters as well as the radar height above the surface and the rough surface statistics. At nadir, the expression is

$$\frac{\sigma_{non}^0}{\sigma_{coh}^0} = 2(kl)^2 \beta_{plf}^2 \sum_{m=1}^{\infty} \frac{k_0^m}{m!m} \quad (20)$$

where $k = 2\pi/\lambda$, $k_0 = 4k^2\sigma^2$, and β_{plf} is the one-way half beam width (β_{plf}^2 is equal to $c\tau/H$). Note that the ratio becomes independent of the surface reflection coefficient when this approximation is used.

Figure 7-8 puts into perspective the relative contributions of coherent and noncoherent backscatter to the maximum power in a peaked signal. The upper panel shows the ratio for a satellite-borne altimeter, and the lower for an airborne altimeter, calculated from Equation (20). In each case, the ratio is plotted against $k\sigma$, with isolines of kl . The figure indicates that either component of backscatter can dominate the signal peak, depending on the roughness of the surface and the altitude and system point target response of the radar. For the regime $k\sigma < 1.0$ and $kl \leq 7.0$, the scattering should be predominantly coherent according to Kirchhoff theory. Such surfaces have been measured for artificial ice, labeled (a), and naturally occurring sea ice in the Gulf of Bothnia, labeled (b). Such surfaces, however, are rarely encountered in dynamic regions, where typical rms height and correlation lengths exceed 0.3 and 7.0 cm, respectively (i.e., $k\sigma > 1.0$ and $kl > 7.0$). Based on field measurements, the noncoherent component approaches and can exceed the coherent component in the roughness regimes of the Beaufort and Labrador Seas, labeled (c) and (d).

In Figure 7-8(a), the relevant system parameters are selected for the ERS-1 altimeter. Results indicate that it is likely that a dominant coherent component will be observed in the waveform peak over most consolidated ice surfaces except those such as in rough ice regime (d). In regimes (a), (b), and (c) the coherent component is more than 5 dB above the noncoherent component. To contrast with the satellite

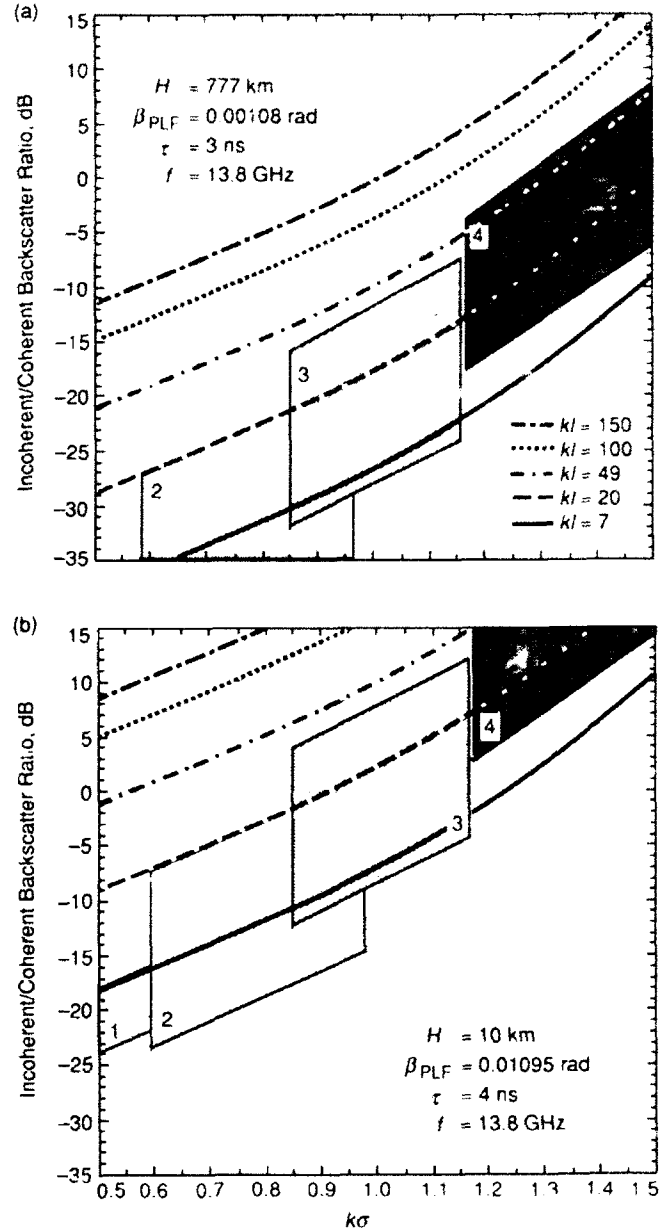


Fig. 7-8. Incoherent/coherent ratio for (a) spaceborne (ERS-1 altimeter) and (b) airborne (RAL altimeter) platforms. The labeled areas correspond to ice roughness regimes measured in several experiments: 1 = CRRFLEX, $0.29 < k\sigma < 0.58$, $2.9 < kl < 8.7$; 2 = BEPERS, $0.58 < k\sigma < 0.97$, $1.2 < kl < 19.5$; 3 = Beaufort'90, $0.85 < k\sigma < 1.16$, $5.8 < kl < 34.7$; and 4 = LIMEX'87, $1.19 < k\sigma < 12.8$, $11.6 < kl < 66.5$.

situation, Figure 7-8(b) demonstrates that the simple increase in the antenna PLF beam width of the airborne altimeter results in increasing dominance of diffuse or noncoherent backscatter. Evidently, only in the smoother regimes of ice roughness will the coherent component approach or exceed the noncoherent returns. This may occur over calm ocean surfaces in marginal ice zones, over frazil slicks or smooth new ice sheets such as nilas, or even during summer melt, when maximum melt pond coverage is achieved. Under calm wind conditions melt ponds provide extremely effective specular reflectors.

Typical waveforms from the RAL altimeter show distinct examples where the peaked component in the waveform does dominate the diffuse component [Drinkwater, 1987; 1991], even in circumstances where the majority of ice is relatively rough. This cannot easily be explained by the simplified arguments presented above, because the ice surface in those cases is assumed to be uniform in its characteristics. Obviously there are situations where phase-coherent returns can occur from rough surfaces with mixed reflection coefficients and roughness scales. This idea is applied to a case of quasispecular RAL altimeter signals where the ratio of coherent to noncoherent powers is of the order of 25 dB [Drinkwater, 1987; 1991]. Such signals are shown to originate in areas of smooth open water between floes (such areas have a reflection coefficient about 10 dB greater than that of ice), and areas of new ice growth. For mixtures of specular ocean and diffuse ice scattering, the areal proportion of smooth ocean required to produce this type of signal is less than 1% [Drinkwater, 1991]. At least in the marginal ice zone, the dominant scattering mechanism therefore appears to be coherent reflection from smooth water between floes, or from new ice growth where centimeter-scale waves are damped out. Similar examples of extremely strong signals exceeding 30 dB (and often reaching 40 dB or more) have been observed in satellite altimeter measurements by both Ulander [1987b; 1991] and Laxon [1989]. Robin et al. [1983] calculated that only 0.01% of the surface within the PLF need be smooth to produce a characteristically peaked satellite waveform.

Given the importance of open water to waveform shape and power, it is necessary to understand under what conditions areas of open water might produce coherent returns. Long wavelength swell is almost completely damped out within a few tens of km of the ice edge. Shorter wind waves are damped in a short distance, on the order of km, but may be regenerated by wind in areas of open water [Wadhams et al., 1988]. Wadhams [1983] calculated the short wavelength roughness generated within the pack using

$$\sigma = 0.1265 U_* \frac{X}{g}^{1/2} \quad (21)$$

where U_* is the friction velocity determined from wind speed, X is fetch, and g is the acceleration due to gravity. The standard deviation of surface height versus fetch for various wind speeds, calculated from Equation (21), is

shown in Figure 7-9. Figure 7-9 illustrates how wind speed can determine whether an area of open water of a given width will appear coherent to the altimeter. For a frequency of 13 GHz, this requires that σ be less than 2.88 nm to meet the Rayleigh criterion, or less than 0.72 mm to meet the more stringent Fraunhofer criterion. Although these relationships are only approximate, they at least give a first-order indication of the circumstances under which open water within the pack is likely to produce a near-specular return.

To conclude, the scattering mechanism for the narrow-peaked waveforms observed by altimeters has been a rather controversial issue in the past. There are not enough measurements of the surface roughness of ice at mm scales to provide a solid basis for theory. Investigators have arrived at different conclusions: that the waveforms originate from true specular reflection [Shapiro and Yapice, 1975; Eom and Boerner, 1986] or from quasispecular noncoherent scattering [Robin et al., 1983; Rapley, 1984; Drinkwater, 1987]. The latter explanation assumes that the rms surface slope is small (less than the angle subtended by the PLF), such that the angular extent of the scattering is confined to within the altimeter angular response. It turns out that the effective backscattering coefficient for the two cases in fact agree, as noted by Robin et al. [1983]. This implies that it is impossible to unambiguously determine the scattering mechanism from waveform data alone [Ulander and Carlström, 1991].

One approach to resolving the question for sea ice is to compile probability density functions of echo energy over example areas. If the scattering is noncoherent, the probability density functions (pdfs) will result in a Rayleigh distribution. If indeed coherent returns are occurring, the pdfs will be more Gaussian in nature. The compilation of such pdfs should be undertaken for a variety of instruments of differing operating parameters (frequencies and beam widths) in order to establish the principal effects. Alternatively, it should be possible with an airborne system

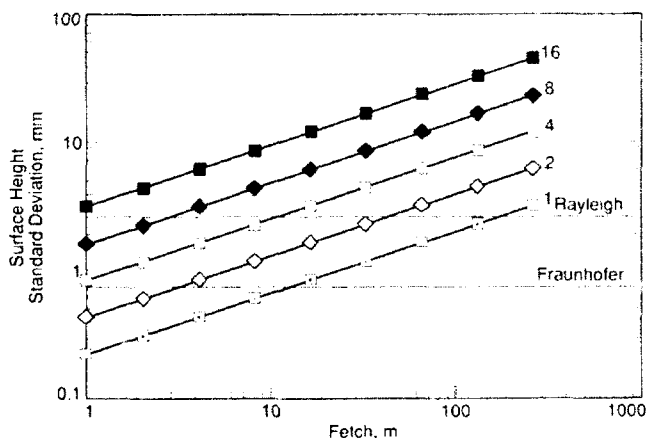


Fig. 7-9. Standard deviation of surface height versus fetch for wind speeds from 1 to 16 m/s. The cutoffs for the Rayleigh and the more stringent Fraunhofer criteria for a smooth surface are shown.

to overfly the same surface at different altitudes. This will enable the range dependency in the scattering signature to be evaluated and thus the scattering mechanism to be resolved completely. Comparing airborne and helicopter-borne results is an alternative method of analysis.

Note that the dependence on altitude in Equations (11) and (12) implies that it may be difficult to compare spaceborne and airborne measurements if a coherent component is present. Typically, the altitude of an airborne altimeter is two orders of magnitude less than that of a satellite, which reduces the coherent component from that measured by a satellite altimeter by about 20 dB. The noncoherent component, on the other hand, is unchanged.

Realistically, in considering coherent reflection one must acknowledge that many returns with different tracker biases or tracker jitters are added together to produce a mean satellite waveform. This inevitably results in a waveform which is the equivalent of the random superposition of mixed coherent and noncoherent components of the return signals. The fading of signals occurring between independent along-track views of the surface facets will inherently lead to some mis-superposition of pulses and thus noncoherent averaging of the signals during the tracking process.

7.4 THEORY VERSUS MEASUREMENT

7.4.1 Surface Measurements

To improve the retrieval of geophysical information from altimetry, it is necessary to better understand what an altimeter is sensing. Answers to questions such as—Where is the signal originating? and What are the effects of snow depth and ice type on backscatter? can be provided by surface measurements. Near-surface backscatter measurements from the Fram Strait marginal ice zone (MIZ) have been acquired at frequencies of 5.25, 9.6, 13.6, and 16.6 GHz using a frequency-modulated continuous-wave radar scatterometer with pencil-beam antenna patterns (two-way beam widths of 1.5° to 4.5°). The radar scattering coefficients were determined by comparing surface returns with returns from calibration targets of known radar cross section. These observations were made from a helicopter in conjunction with surface observations that allow backscatter to be related to a particular ice type or to ocean conditions [Onstott, 1991; Onstott et al., 1987]. Also given in this section is a synopsis of recent measurements in the Weddell Sea.

7.4.1.1. Vertical incidence scatterometer data from the Fram Strait marginal ice zone. The four major ice types present when the measurements were made in midsummer were multiyear (MY), thick first-year (TFY), medium first-year (MFY), and thin first-year (ThFY). Snow depths for MY and FY ice by midsummer were about half of what they were at the beginning of summer. This is important in that thick ice, such as TFY and MY ice, will have enough snow cover to mask much of the ice surface from microwave

radiation for at least half of the two-month-long summer. Data were acquired by flying scans from a position over the ocean about 20 km from the ice edge, across the ice edge, and into the MIZ until large floes were encountered (an additional 20 km). One such transect is shown in Figure 7-10. Illustrated in these data is the transition from the strong backscatter of the open ocean, to a region of calm water (5 km in extent) immediately adjacent to the ice edge, through a well-delineated and compact ice edge, into a region with bands of similarly sized ice floes and varying ice concentration, and then into a region of 90% ice concentration and large multiyear floes.

Using the open ocean signature as a reference, the area of dead water near the ice edge produced an enhancement of about 6 dB. Backscatter from ice is dramatically smaller (by 8 to 21 dB), in contrast to the usual observations by airborne and satellite altimeters moving from ocean to MIZ. This difference may be explained by the much larger Fresnel zone of airborne and satellite-borne instruments, which can encompass flat areas, with a resulting dominance of coherent reflection. As the ice concentration increases deeper in the MIZ, a lower average return is observed. The strongest returns are associated with the water between floes. These returns are specular in nature and are characterized by a cross section at vertical of greater than 25 dB and a reduction in intensity of almost five orders of magnitude by 25° . These results support the assertion that peaked returns in airborne and satellite data come from smooth water between floes. The range of scattering coefficients is also of interest. The range for the open ocean is about 6 dB, whereas in the MIZ it is about 40 dB. The high range in the MIZ is due to the presence of areas of open water, which produce a variety of microwave signatures influenced in large part by their position from the ice edge (Figure 7-11). Outside and within the ice edge, variations in ocean surface roughness are caused by complicated interactions between wind, waves, currents, and fresh water input. These interactions are driven by effects related to cold air from the pack

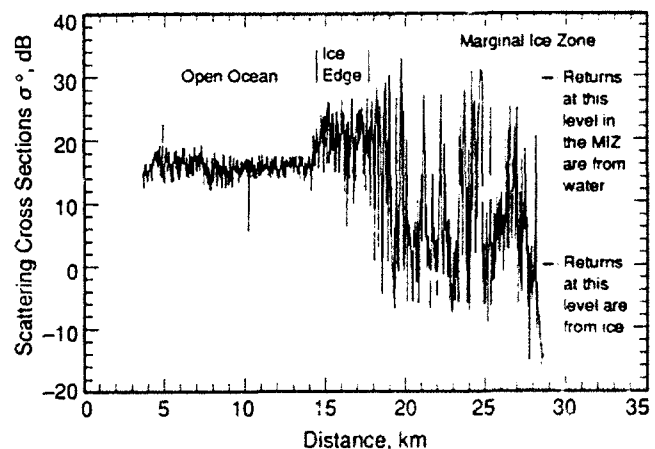


Fig. 7-10. Measurements from a single radar scatterometer transect across the ice edge on July 5, 1984 at 13.6 GHz and a vertical incidence angle.

crossing from the cold ocean ice and sea surface temperature of 0° to 2.5° C) near the ice edge to the warmer open ocean (sea surface temperature of 4-4° C). One result of this movement of cold air is the area of calm water adjacent to the ice edge.

The transition from the open ocean to the calm water within the MIZ is very rapid in this case. It occurs within 600 m, and it produces large level shifts in backscatter. This sharp delineation was observed often during MIZEX'83 and '84. Ambiguities or errors in detecting the ice edge with altimetry may occur if the ocean near the ice edge damped by a cold air mass is mistaken as an ocean surface damped by a thin layer of ice. In the satellite case, the ice edge is marked by a similar increase in variability but higher backscatter values over the ice.

The MIZ is a dynamic region. Diffuse scattering from deformed ice is observed to produce returns 12 dB below that of flat ice. Returns from water in the shadows of floes are 2 to 5 dB above typical ocean returns from within the MIZ. Backscatter modulations are also found to be a function of ice concentration and, to a lesser extent, floe size. Based on other observations by Onstott, the backscatter response for winter is anticipated to be very similar. The distribution of features within the boundaries of a floe may also have an important impact on the backscatter response. Pressure ridges, melt ponds, and the blocks that pile around the floe edges require consideration. New pressure ridges may form at floe boundaries and are differentiated from older pressure ridges that may be covered with a layer of wet snow. P ridges result in weak backscatter, with the more recently formed ridges producing the more diffuse scatter response. Pools, often small and protected from wind by undulating ice, were found to produce backscatter cross sections of a magnitude similar to that of shadowed water signatures. On July 5, when these observations were made,

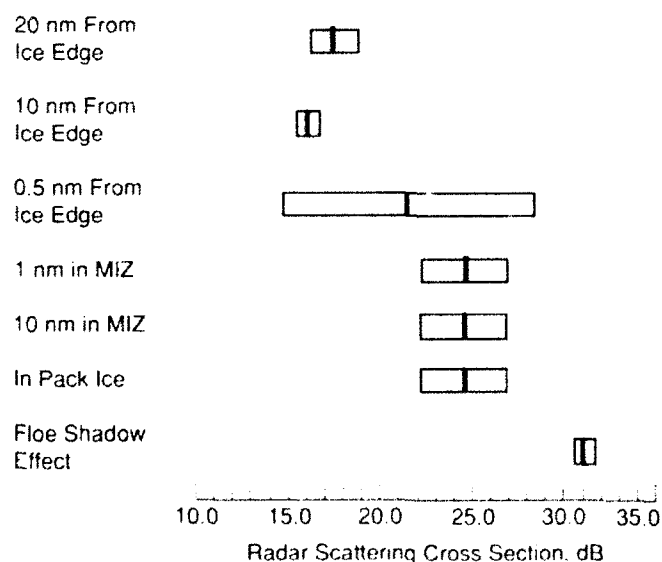


Fig. 7-11. Liquid ocean radar scattering cross sections shown as a function of position from the ice edge at 13.6 GHz and a vertical incidence angle.

minimal floe area was covered by melt ponds. Melt pond formation was, however, under rapid acceleration and by July 9, coverage on MY floes was estimated at about 50%.

7.4.1.2. Ice type and feature discrimination in Fram Strait measurements. During summer, the reflectivity at nadir of FY and MY ice is determined by the presence of moist snow, the areal extent of melt ponds, and topography. Melt ponds increase the reflectivity of a floe, and topography acts to reduce the intensity of the reflection. At 13.6 GHz, the reflectivities for the three primary ice types are within a very narrow 4.5 dB range. Table 7-1 shows that the backscatter response follows, in large part, surface topography. Thin first year ice is characterized by the thinnest snow cover (mean of 4 cm) and is tabular, with little if any deformation. It produces the largest reflectivity of the three ice types. Physically, MFY ice is similar to ThFY ice, except that it has a thicker snow cover (mean of 10 cm). MFY and MY share a similar signature, that of an ice sheet with a very thick snow layer. The data at 13.6 GHz for snow-covered MY appear high at first glance, but upon further examination they are consistent with the other observations shown in Table 7-1. A MFY floe produced a signature 3 dB lower than that of ThFY, where snow was about 10 cm. On the same MFY floe, however, there was a region where snow had accumulated to 14 cm. Here the reflectivity increased to 8.0 dB. This is identical to the reflectivity observed on the MY ice and within 1.2 dB of that of ThFY ice. Thick snow on the MY ice, rather than the snow-ice interface, dominates the MY signature.

While backscatter for winter and summer FY ice is very similar, significant differences in the seasonal response of MY ice are observed. These are related to the moisture contained in the snow and ice sheet [Onstott et al., 1987]. Moisture limits the penetration into the ice sheet, thereby reducing or negating the volume scattering that dominates the backscatter response of MY ice during winter. At vertical incidence, this causes a 9-dB signature enhancement (at 13.6 GHz) for MY ice during summer when compared to the winter response. Measurements of snow moisture show that the bulk wetness of the snow pack is about 5.5% by volume, and the majority of the snow pack is

TABLE 7-1. Radar scattering coefficients at vertical incidence angles expressed in decibels. Measurements were obtained July 5, 1984, in the marginal ice zone [Onstott, 1991].

Scene	Frequency, GHz			
	5.25	9.6	13.6	16.6
Ocean, open	13.3	14.5±1.6	15.9±0.7	
Ocean, edge		17.4±2.4	21.5±6.9	
Ocean, interior	31.3±10.1	22.8±22.6	24.5±2.4	
Thin FY ice	2.0±1.2	6.4±9.4	9.2±6.8	8.9±5.9
Medium FY ice	-0.8±2.4	2.9±3.0	4.7±3.9	7.0
MY thick snow	-1.3±3.0	2.6±4.0	7.9±3.9	6.1±5.0
MY with melt pools	10.4±8.2	8.3±9.8		

old and has a density of 400 to 500 kg m⁻³ [Onstott et al., 1987]. The penetration depths calculated for these conditions are about 4.5 cm, 1.8 cm, 1.5 cm, and 1.3 cm, for 5.25, 9.6, 13.6, and 16.6 GHz, respectively. The snow pack on MY ice up to midsummer may be 40 cm. Note that at 13.6 GHz, only 1 to 3 cm of snow is required before the snow layer completely dominates the backscatter response since for each penetration depth the incident signal experiences a 9-dB round-trip loss.

7.4.1.3. Shipborne Ku-band radar observations in the Weddell Sea. Ku-band radar data were acquired during a transect of the R.V. *Polarstern* through the Weddell Sea during the austral winter of 1989 [Lytle et al., 1992]. A VV polarized network analyzer-based radar developed at the University of Kansas made observations at incidence angles spanning 0° to 30°. Most radar data were acquired on ice floes against which the ship was moored. Measurements of physical properties of the sea ice included surface roughness, snow cover thickness, snow and ice density, and grain size and salinity. Ice freeboard data were also collected by drilling numerous holes through the ice and measuring water level relative to the ice surface.

Flooding at the ice-snow interface seems to be a characteristic phenomenon of the western Weddell Sea [Lange and Eicken, 1991; Wadhams et al., 1987]. This process is apparently associated with enhanced snow accumulation depressing the ice surface below sea level. Flooding changes density and salinity in the lower parts of the snow layer, which in turn affects the radar response. Backscatter is plotted against freeboard and parameterized against slush layer presence in Figure 7-12. Backscatter is elevated when a slush layer is present, presumably because of the enhanced dielectric contrast. Flooding, then, may be another mechanism for situating a relatively bright target within the radar footprint. The possibility of flooding must be taken into account when attempting to interpret altimetry in terms of ice concentration or type. Laboratory measurement to further study the importance of flooding are described in Chapter 9.

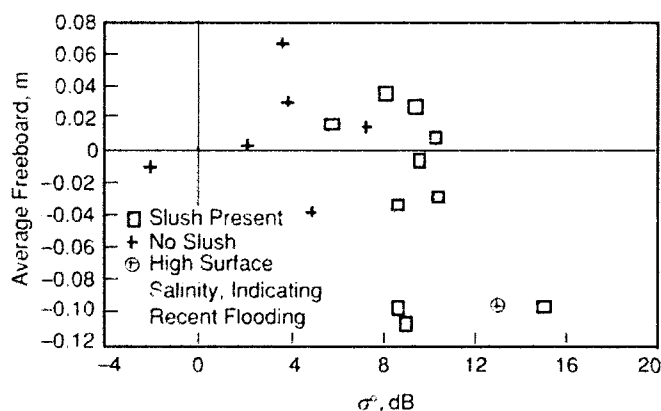


Fig. 7-12. Average ice freeboard versus σ^0 parameterized against the presence of a slush layer.

7.4.2. Aircraft Measurements

Various work [McIntyre et al., 1986; Drinkwater, 1987; Fedor and Walsh, 1988] has documented the characteristics of airborne altimeter waveforms over mixtures of sea ice and water. Several of these studies [Powell et al., 1984; Cowan and Squire, 1984] document results from a pre-launch campaign for ERS-1, in which the RAL altimeter acquired data in experiments devised to indicate the characteristics of sea ice relevant to altimeter pulse analysis. Airborne altimeters generally have wider beams than satellite altimeters, in order to reduce the impact of antenna off-pointing caused by aircraft motion. A wide beam leads to different waveform characteristics than are observed with a satellite-borne instrument, as was discussed in Section 7.3.2. The surface area sensed by an airborne instrument is usually a factor of 100 smaller than for a satellite altimeter, while it subtends a wider range of incidence angles. This is a critical difference, because in areas consisting of mixtures of ice and water there is inherently a larger area of water available to the satellite altimeter for scattering from nadir than is available to the lower altitude airborne instrument. Another consequence of the airborne altimeter's wider beam is that backscatter fall-off with incidence angle can be measured.

7.4.2.1. Waveform examples. Figure 7-13 is an example of the operation of the RAL altimeter over a variety of sea ice conditions in the marginal ice zone of the Fram Strait. Consecutive waveforms exhibit dramatic changes in proportion as the instrument passes over large ice floes and areas of open water in the pack. Note that some waveforms show saturation. One interesting finding illustrated by the waveform labeled *a* is that as the altimeter passes over a lead only a few meters wide, the altimeter responds extremely sharply if the lead is at nadir. Fedor and Walsh [1988] noted the same phenomenon in data from the Beaufort Sea. Since the power reflection coefficient of water is generally 11 dB higher than that for snow-covered sea ice, the water between ice floes dominates the backscattered signal near nadir. Other observations from this data set show that when the sea ice fills the footprint, waveform shape becomes suggestive of ocean returns as the signal level is modulated by the type and surface roughness of sea ice present. Fedor et al. [1989] note typical peak backscatter strengths of around 30 to 37 dB over areas of new sea ice and around 10 dB over deformed FY ice in the Beaufort Sea. These observations show close correspondence with the findings of Drinkwater [1991] over FY ice in the Fram Strait. In the latter study, accompanying surface measurements [Tucker et al., 1987] led to attempts to classify ice types using the altimeter waveforms. The study revealed four distinct surface classes based on surface roughness (or fall-off of backscatter with incidence angle) and normal incidence backscatter coefficient. These corresponded in near-coincident SAR images and aerial photographs with smooth, bare FY ice with minimal ridging; snow-covered FY

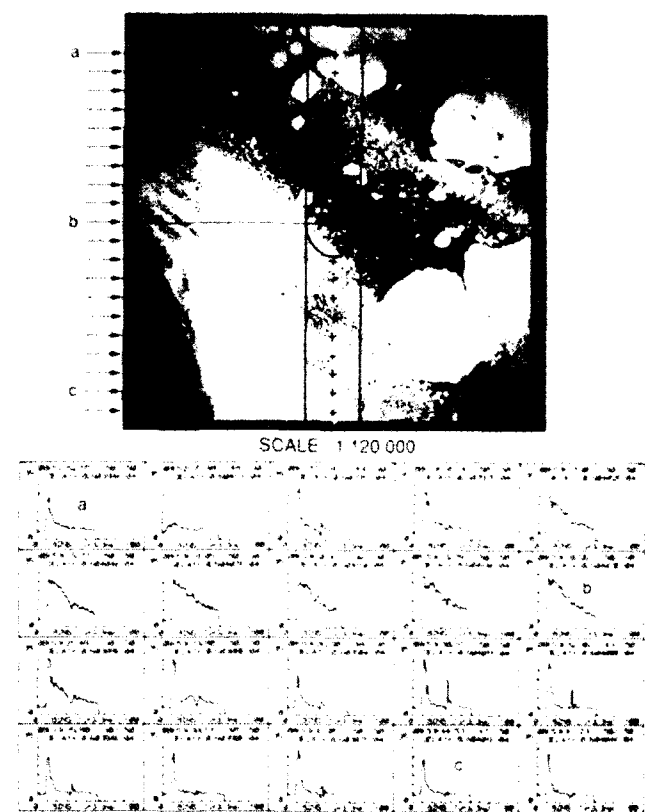


Fig. 7-13. MIZEX'84 RAL airborne altimetry over mixed ice concentrations in the Fram Strait. Waveforms show received power in range gate bins [Drinkwater, 1987].

ice; rotted, rough conglomerate ice floes; and MY ice with large-scale surface roughness.

In ice-water mixtures, the rapidity with which the power decays after the peak is largely a function of the wave slope (see Section 7.3.4). Some areas, such as for waveform *b*, provide non-fetch-limited regions of almost open water within the pack. Wind-generated gravity and capillary waves develop rapidly in the absence of floes (unlike at *c*). The waveform trailing edge responds dramatically to the presence of these waves and particularly to the higher wave slopes. The waveforms become more ocean-like, albeit with a relatively high normal incidence backscatter coefficient due to the lack of large gravity waves.

Volume scattering cannot be neglected when old ice has low-density, bubbly upper layers (Chapter 2). Volume scattering leads to a backscatter response function that tapers much more gradually with incidence angle. It is suggested as a mechanism for some Fram Strait observations where neither the rms surface roughness nor the residual aircraft motion can account for the spreading of the waveform leading edge. Together with the large-scale surface roughness observed on vast low-salinity MY floes, volume scattering appears to result in rms tracker delay variability or height fluctuations of between 0 and 4 m [Drinkwater, 1991]. The snow depth on these floes averaged 28 cm, and ridge sail heights varied between 3 and

5 m. In contrast, over large FY floes the measured rms surface height variability was less than 1 meter, and such tracking excursions were not noted. For the same effects to occur in satellite data, the radar would likely have to be directly over a vast MY ice floe or iceberg. This situation would be encountered in the Arctic during winter conditions and in the Antarctic, where vast tabular icebergs are often observed by altimetry [McIntyre and Cudlip, 1987; Laxon, 1989; and Hawkins et al., 1990].

7.4.2.2. Ice concentration derivation from airborne observations. Attempts have been made to use altimetry for ice concentration measurements. The models described in Section 7.3.3 yield fractional areas of smooth ice and open water facets, if reflection coefficient and size are specified. These do not, however, incorporate the slope distribution, which is portrayed for both ice floes and the water between in the heuristic model in Figure 7-14. This model illustrates the decline in significant wave height caused by sea ice wave attenuation [Rapley, 1984] and the associated decline in wave slope as short wavelength waves are preferentially damped. The resulting modulation of the waveform power directly from ice concentration will therefore vary as a function of both rms wave height and fractional coverage of sea ice (based on the premise that the returned power in the waveform decays as the ratio of low-reflectivity ice to high-reflectivity water increases). Figure 7-14 shows idealized waveforms at concentrations of 0, 20, 40, 60, 80, and 100% for a given wave regime. In each case the total height distribution is a combined effect of wave height, ice surface roughness, and penetration, while the form of the waveform trailing edges is a result of the wave slopes observed between ice floes.

Using altimeter data over ocean surfaces inside the MIZ edge, Drinkwater [1987] shows that the angular backscatter scattering function is predicted by noncoherent geometric-optics theory. The model fit to the data gives an rms

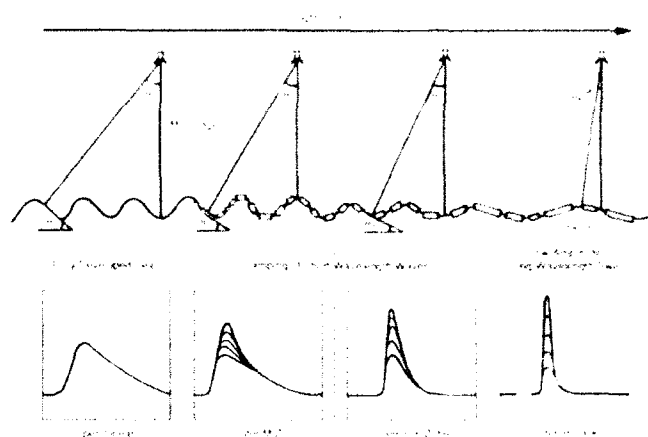


Fig. 7-14. Waveforms generated by heuristic model of wave decay with attenuation, and families of waveforms associated with varying ice concentration: 0, 20, 40, 60, 80, and 100% [Drinkwater, 1987].

slope 12.8° . This is consistent with waves measured in the ice edge for a fairly well-developed sea. With increasing distance into the MIZ, observations show a corresponding decrease of rms slope to around 3° at 40 km from the ice edge. The progressive damping of ocean waves as they pass into the MIZ results in more and more spiked echoes from the water between ice floes, as shown in Figure 7-14. Thus, waves and the wave spectrum in the MIZ mutually interact with the shape and strength of altimeter signals and must be considered when attempting to derive concentration from waveforms. In an analysis of the relationships between backscattered power and ice concentration in the Greenland Sea, Drinkwater [1991] investigates airborne Ku-band signals for which there are accompanying SAR and photography data. To obviate the requirement for compensating wave height information, altimeter waveforms are chosen beyond the point at which they are modulated by waves. These are subsequently compared with digitized, simultaneous aerial photographs over a track length of 130 km. Both the peak backscattered power and integrated power in the trailing edge of the waveform are shown to be related to the ice concentration. However, because of the saturation effects found in these data, the peak power could not be used for accurate ice concentration retrievals. The waveform integral, on the other hand, declines monotonically with increasing ice concentration and is reasonably robust. Regression analysis shows that the relationship between these two variables had a correlation coefficient of -0.81 , and 65% of the signal energy variance is accounted for using this measure alone. The rms residual error is 13%, and the remainder of the variance is accounted for by varying surface conditions due to local wind roughening, varying ice types, ice roughness, and other factors.

7.4.3 Satellite Measurements

A common problem in the analysis of altimetry is to find high-quality surface truth data with which to determine ice conditions during the sensor overflight. For corroborating the interpretation of satellite altimetry the most successful data source has been SAR [Swift et al., 1985, Ulander 1987a, Fetterer et al., 1991, Ulander and Carlström, 1991]. Examples of investigations that rely on SAR are given in this section. Comparisons of altimetry with imagery from passive sensors is reserved for Section 7.4.4.

7.4.3.1. Echo waveform simulations compared with measurements. We noted earlier that it is impossible to determine unambiguously the scattering mechanism from a single narrow-peaked waveform. However, a series of such waveforms may provide this information as the altimeter moves from a smooth area into an adjacent area with diffusely scattering characteristics. For true specular reflection, the returned power essentially originates from the first Fresnel zone. This implies a horizontal resolution according to Equation (9), which is almost an order of magnitude finer than the pulse-limited resolution for an ERS-1 class altimeter. Hence, the echo waveform will, in

the specular case, respond more quickly to a change from a narrow-peaked to a diffuse type of scattering.

This observation has been used to determine the scattering mechanism of narrow-peaked waveforms over sea ice in the Baltic Sea [Ulander and Carlström, 1991]. A section of Geosat altimeter data was extracted over a newly frozen lead surrounded by very deformed ice. The former produced narrow-peaked waveforms and the latter essentially diffuse waveforms. A pulse echo series was then simulated by integrating over the illuminated surface at each platform position along-track, and an echo waveform was produced by averaging over one hundred pulse echoes. The surface composition is shown in Figure 7-15(a). It was derived from a high-resolution airborne SAR image that delineated the two surface types. Figure 7-15(b) shows the Geosat normal incidence backscatter coefficient and two simulations that assume a coherent and noncoherent mechanism, respectively. In the noncoherent simulation, the young ice was represented by a model according to Equation (17), whereas in the coherent simulation all the returned power originated from the first Fresnel zone with uniform weighing. Note the close agreement between the Geosat data and the noncoherent simulation. The model parameters in Equation (17) were chosen as $F = 3.3\%$ and $\theta_D = 0.068^\circ$ (for $D = 5.5$ m). The coherent simulation, on the other hand, shows a much higher sensitivity to the changing surface characteristics than does the Geosat data. This particular example shows that the narrow-peaked waveforms over the frozen lead, corresponding to a high backscatter coefficient of 32 dB, were indeed noncoherent in nature. The backscatter value over the lead in Figure 7-15(b) is somewhat less due to distortion by the pulse echo simulation and waveform averaging.

The remaining issue to resolve is whether the noncoherent scattering is in accordance with the geometrical optics or flat patch model. Both models predict a backscatter coefficient of the same functional form and have essentially the same effective backscattering coefficient for narrow-peaked waveforms. Note, however, that the cause for the angular response is quite different. In the geometrical optics model it is determined by the rms surface slope, since the reflecting specular points are infinitely large compared to the wavelength; in the flat patch model it is determined by the flat patch diameter since the patches are assumed horizontal (i.e., with zero surface slope). There are, as yet, no field measurements which could help resolve this question. In general it would require that the joint height probability density function be determined for scale lengths between 1 cm and 100 m. Hence, our effort in the future must turn toward more sophisticated field measurements of the surface roughness.

7.4.3.2. Ice type signatures in satellite measurements. With an approach quite different from that outlined in Section 7.4.2 for airborne altimetry, Chase and Holyer [1990] extend the measurement of ice type and concentration to satellite altimetry. Their work uses a linear unmixing model, suggested by the fact that waveforms from the MIZ

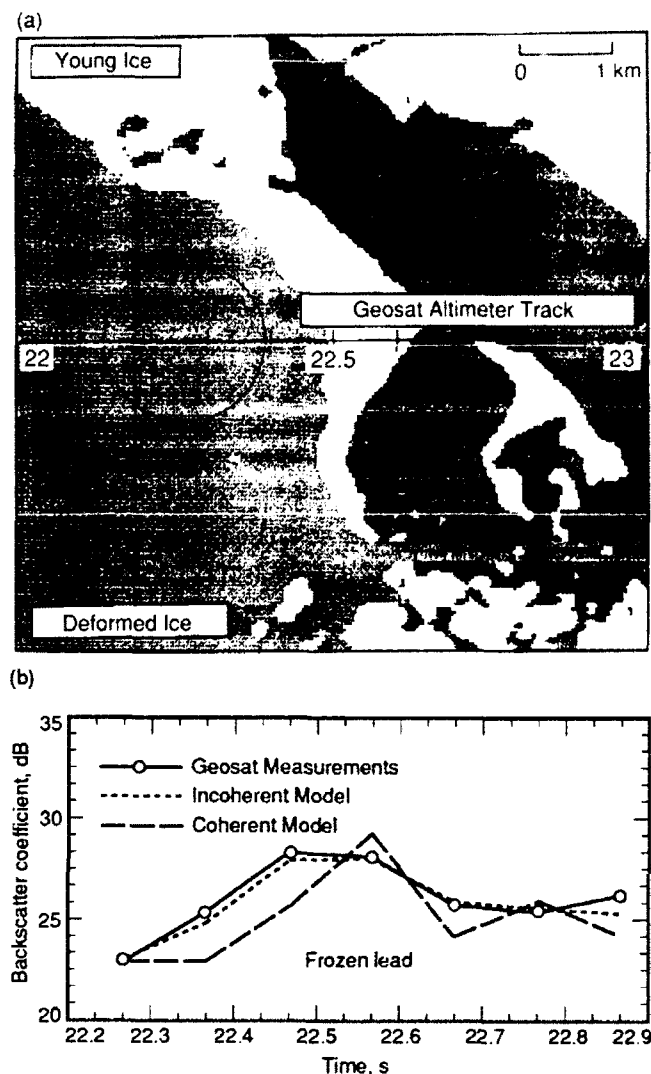


Fig. 7-15. (a) Simulated surface composition derived from an airborne SAR image of Baltic Sea ice, and (b) simulation result compared with Geosat measurements [Ulander and Carlström, 1991].

and pack are usually the result of backscatter from mixtures of ice and water in the footprint. Each waveform is represented as a multidimensional vector that can be expressed as a linear combination of end member vectors. Analysis consists of identifying the end members and associating each with a surface type. Although the model can be adapted for nonlinear combinations of waveforms, Chase and Hoyer argue that it is not necessary for the data they examined. Using manually interpreted airborne passive microwave imagery collected in the Greenland Sea within hours of a Geosat overpass, Chase and Hoyer found that the analysis of the concentration of three combinations of types (open water and brash ice, FY and old ice, and young and new ice) agreed with that from the passive microwave analysis to within 4.6% over the experiment area. Interestingly, the shape of the end member paradigm

waveforms suggests that concentration in this analysis is directly proportional to peak power and waveform integral. Possible explanations for this contrast with the airborne case are the differences in scale and range discussed in Section 7.3.2.

Most investigations of the ability of satellite altimeter measurements to distinguish between broad ice thickness classes and to detect water openings, starting with that of Dwyer and Godin [1980], have only used the altimeter data in a relative sense. This is because the data lack absolute radiometric calibration. It should be emphasized that it is only possible to obtain an effective backscatter coefficient when the angular waveform is narrow peaked. By assuming a particular form of the angular response, it may then be possible to obtain a better estimate of the backscatter coefficient at normal incidence. This inherently assumes that the system impulse response is sufficiently narrow to resolve the angular scattering response and that the scattering mechanism is known.

The correlation between radar backscatter at normal incidence and Arctic and Baltic winter ice types has been described by several investigators [Ulander, 1987a, 1988; Fedor et al., 1989; Ulander and Carlström, 1991]. Histograms of the normal incidence backscatter coefficient for some of these ice types are shown in Figure 7-16. The normal incidence backscatter coefficient decreases in general for increasing ice thickness, such that new ice has the highest values (30 to 40 dB) and MY ice the lowest (10 to 20 dB). Very deformed ice also has a low backscatter coefficient (10 dB). Note the high mean values for all classes when compared with the surface measurements of Section 7.4.1. These results suggest that broad ice classes can be inferred from the altimeter backscatter data, provided the surface conditions do not change rapidly along track. When the latter is not the case (for instance in the MIZ), the signature shows a large variability, which introduces difficulties in the interpretation.

Figure 7-17 shows curves of the backscatter coefficient and the echo waveform width (a measure of diffuse scattering) for a Seasat altimeter track in early October off the coast of Alaska [Ulander, 1987b]. The curves are overlaid on a Seasat SAR image that was acquired a few hours earlier. Narrow, peaked waveforms dominate over the pack, except where the nadir track crosses two large floes. Figure 7-18 shows a similar comparison of Geosat altimetry and airborne SAR in the Greenland Sea [Fetterer et al., 1991]. Here, however, the high-frequency variability in backscatter is much greater. Backscatter is from the 0.1-second waveforms. Note that AGC is a somewhat smoothed version of peak power. The voltage proportional to attitude, or VATT parameter, is a measure of power in later gates. Low values of VATT (plotted every second) indicate peaked returns. The parameters in Figure 7-18(c) delineate zones:

1) The MIZ, where backscatter rises from 9 to 30 dB as the ice edge is crossed. Waveforms are strong and peaked, suggesting reflection from water between the small floes, which give a bright return in the SAR image. Backscatter

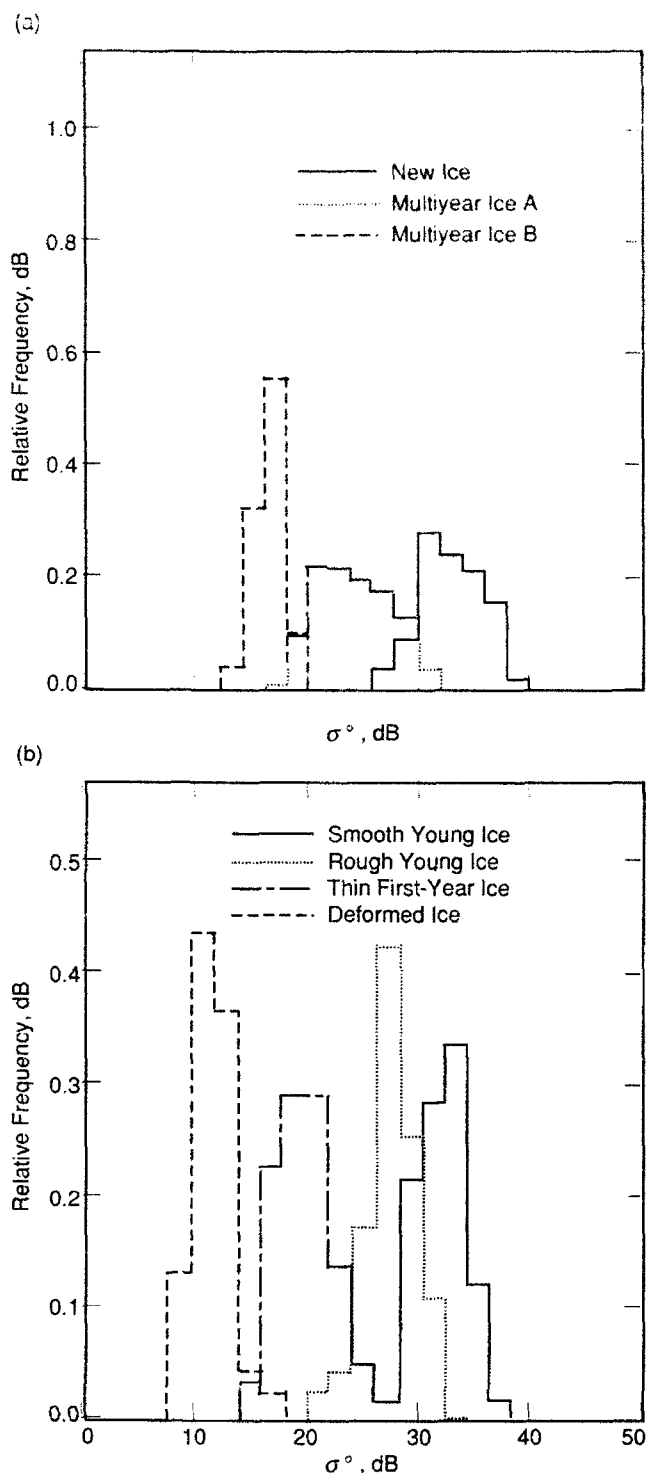


Fig. 7-16. Backscatter histograms for (a) Beaufort Sea ice from Seasat data [Ulander, 1988], and (b) Baltic Sea ice from Geosat data [Ulander and Carlström, © 1991 IEEE].

drops slightly over an expanse of open water several kilometers wide, where wind may roughen the surface.

2) The pack, where variability is high. Backscatter is somewhat lower in the western half, where there is a larger percentage of rough ice. Backscatter dips over two large old floes, which appear quite bright in the SAR image.

3) The fast ice, where backscatter reaches its lowest level and waveforms are not peaked but are more characteristic of ocean returns. This is evident in the waveforms plotted in Figure 7-18(a).

While changes in the nature and variability of waveforms are revealing, caution should be taken in interpreting the power and shape of waveforms from an inhomogeneous area such as this in terms of ice roughness or type. Instrumental effects and rapid changes in surface characteristics (described in Section 7.2.5) drastically alter individual averaged waveforms.

7.4.4 Satellite Altimetry Compared With Infrared, Visible, and Passive Microwave Imagery

In Sections 7.4.2 and 7.4.3 aerial photography or SAR imagery was used to gain insight into scattering mechanisms and to test the possibility of deriving concentration and type estimates from altimetry on a case-by-case basis. Further applications arise from the synergistic use of radar altimetry with imaging sensors. For example, if a certain ice type can be identified in imagery, this may aid greatly in the interpretation of the radar altimeter data, which may then be used to measure surface elevation and roughness (derived from waveform leading edge width). This section compares altimetry with wide-swath imagery on the regional and global scales required of operational algorithms. Such comparisons enhance our understanding of the operation of both sensors while aiding the development of altimeter data algorithms. Immediate applications lie in the area of algorithm validation. For example, the altimeter has shown great promise in validating ice extent mapping by passive microwave instruments. In addition, ERS-1 altimeter sea ice products can be validated using data from the ERS-1 Along Track Scanning Radiometer.

7.4.4.1. Waveform parameterization. Figure 7-19 shows the two parameters computed from altimeter waveforms to quantify the response over sea ice in the following analysis. The first, *SIGPK*, represents the peak backscatter measured in the return echo. The second, *SIGTD*, is computed as the difference between the average power in eight early and eight late range gates in the altimeter return. *SIGTD* is essentially a measure of the degree of peakiness in the return echo.

7.4.4.2. Observations of a compact ice edge in the Greenland Sea. The Advanced Very High-Resolution Radiometer (AVHRR) onboard the NOAA series of polar orbiting satellites provides visible and infrared imagery with a swath width of 2900 km and nadir resolution of 1.1 km. It is routinely used for operational ice analysis. Figure 7-20(a)

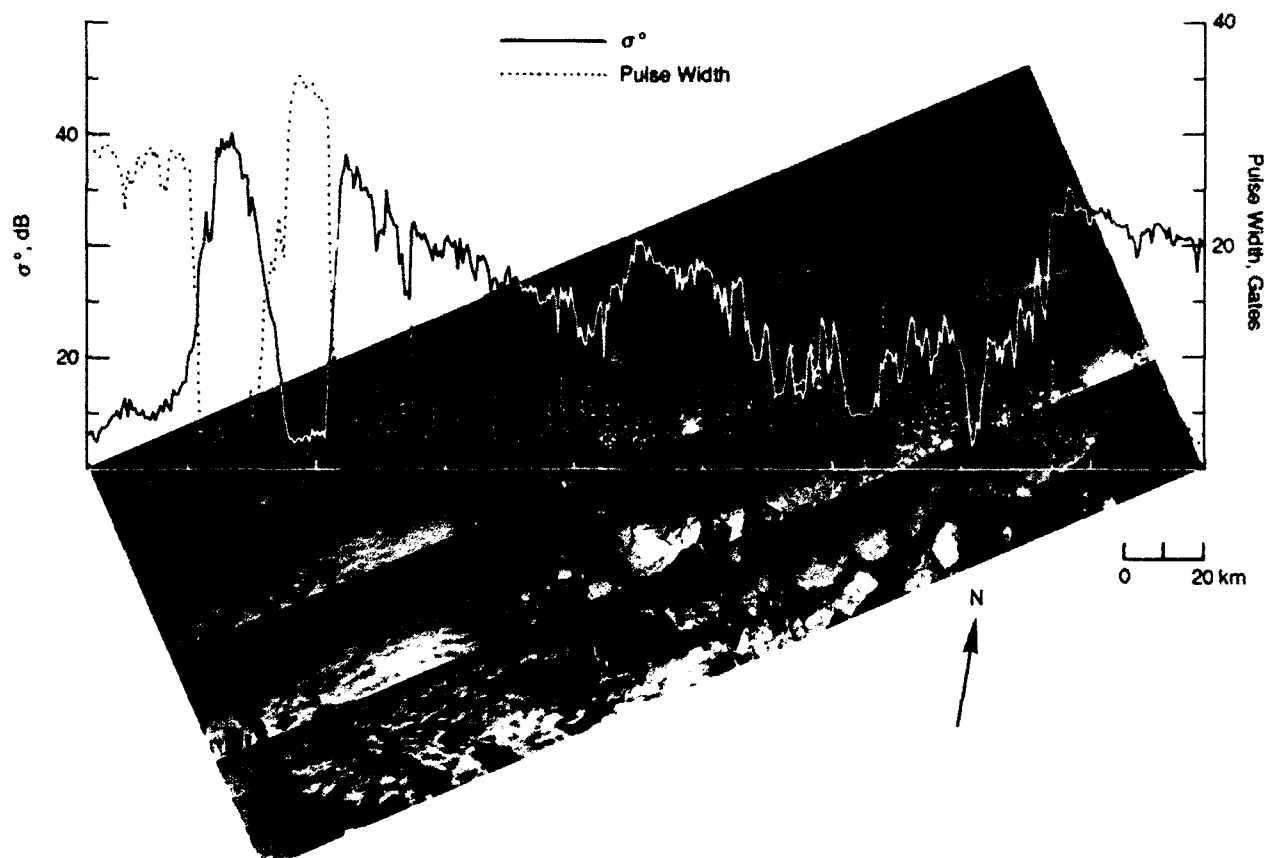


Fig. 7-17. Seasat altimeter measurements in the Beaufort Sea compared with Seasat SAR for October 3, 1978 [Ulander, 1987b].

shows four Geosat altimeter tracks overlaid on a channel 2 (visible band) image of the Greenland Sea. Both altimeter data and imagery were acquired on May 10, 1987. Parameters *SIGPK* and *SIGTD* are derived for every waveform. There is therefore a value every 0.1 seconds, or every 0.7 km along the ground track. A sharp rise in both parameters is observed close to the ice edge visible in the imagery. In some cases, notably tracks B and C, a rise in *SIGPK* is observed outside the ice edge and before any noticeable rise in *SIGTD*. The cause of this is unknown, but the examples demonstrate the sensitivity of the altimeter to the presence of sea ice. A similar rise in backscatter, related to the damping of waves due to the proximity of sea ice, is seen in the surface measurements of Section 7.4.1. The highest strength (with values up to 40 dB) and most peaked echoes are observed just inside the ice edge, which is normally populated by small (<100 m) ice floes. Further into the pack the waveform strength and peakedness decrease and become more variable. This is attributed to a less heterogeneous surface caused by the presence of larger ice floes. In some areas, such as where track A crosses track D, cloud cover can confuse identification of the ice edge. In such cases the altimeter may be used to better identify the location of the ice edge.

7.4.4.3. Observations of a diffuse ice edge in the Greenland Sea. Figure 7-20(b) shows three altimeter tracks overlaid on an AVHRR channel 4 (infrared) image acquired on March 18, 1987. In this instance an off-ice wind results in a more diffuse ice edge than is observed in the May 10 image. The two altimeter tracks labelled A and B show a gradual increase in echo strength over some distance with little increase in echo peakedness. This is attributed to a more gradual damping of ocean waves than is observed in the May 10 image. Again the strongest and most peaked returns are observed further into the ice pack.

Of particular interest in this image are the two large floes observed close to the coast and transected by altimeter track B. The floes are clearly delineated by low strength, ocean-like echoes. Unlike other areas of the pack, where smooth ice or open water can occur within the altimeter footprint, over these vast ice floes the altimeter is observing only a rough ice surface. Such a phenomenon may make it difficult to discriminate between the return from open water and that from a large floe. However, because such surfaces fill the footprint for several waveform integration times, they do provide the possibility of measuring meter-scale roughness and even ice freeboard. The AVHRR image was acquired some 13 hours after altimeter pass B. The southward offset of the two ice floes with respect to the

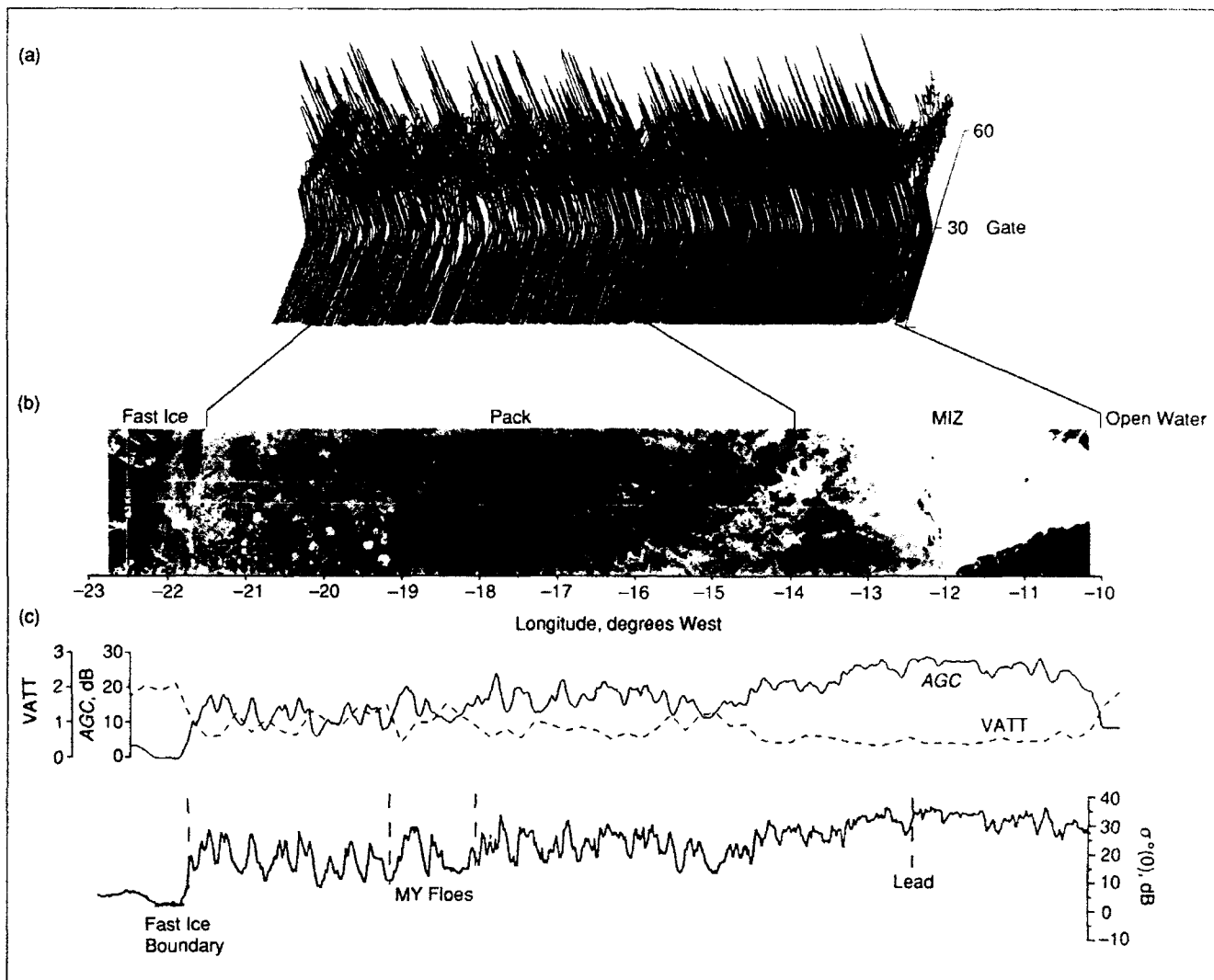


Fig. 7-18. (a) Geosat altimeter waveforms from April 13, 1987, with a (b) near-coincident (within 1 hour) airborne SAR image of the East Greenland Sea at 72° N. White lines on the image mark the approximate position of the 9-km-wide range-window-limited footprint. (c) Measures of peak power, $\sigma^0(0)$, average power, AGC, and waveform shape, VATT, are plotted. Along-track registration of SAR image and altimeter data is estimated to be within 2 km [Fetterer et al., 1991].

signal in the altimetry can be attributed to motion in the East Greenland current.

A similar ocean-like signal is observed over the fast ice, with a sharp decrease in echo strength at the fast ice boundary followed by a slight step increase in echo strength further into the coast. Again this is due to the altimeter observing only a homogeneous rough ice surface. The delineation of two zones within the fast ice suggests that the altimeter is discriminating between an inner zone of fast ice that has survived the winter intact, and an outer, rougher zone that has been broken up at some time by a winter storm. (Similar zonation in the returns from fast ice is apparent in Figure 7-18).

7.4.4.4. Midwinter image of the Kara Sea. Figure 7-20(c) shows three altimeter tracks overlaid on an AVHRR channel 4 image of the Kara Sea acquired on February 21, 1986. Waveform echo data are not available for this period and therefore the AGC values are displayed. In this thermal image, darker areas indicate higher surface temperatures and therefore thinner ice. To the right of the island Novaya Zemlya an area of relatively new ice has formed. On the far right-hand side of the image a further large frozen lead, some 20 km across, is observed close to the continental land mass. For this image, echo strength shows a strong correlation with ice age. New, smooth ice produces stronger returns than older, rougher ice. This phenomenon is exactly what would be expected when considering normal incidence radar backscatter over surfaces with varying

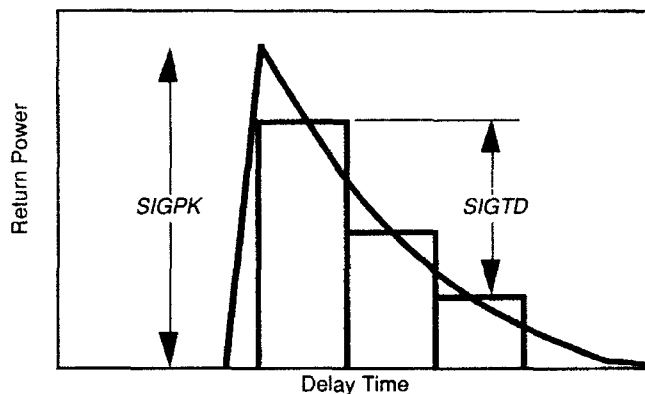


Fig. 7-19. Waveform parameters *SIGPK* and *SIGTD* are measures of the peak power in a waveform and of the peakiness, or rate of backscatter fall-off with incidence angle, in the waveform. *SIGTD* is calculated by taking the difference in average power between eight early and eight late range gates.

degrees of roughness. The highest echo strengths are observed over the narrow lead, which is slightly darker than the ice just east of Novaya Zemlya. Within the older ice some cracks are observed to correlate with individual peaks in the altimeter *AGC* value. In some cases peaks are observed in *AGC* that do not correlate with any cracks visible in the imagery. Smooth ice or open water not resolved in AVHRR imagery are believed responsible for these peaks. These observations demonstrate the sensitivity of altimeter data to areas of thin ice and leads. The mapping of leads has great importance to sea ice research, as leads modify ocean-atmosphere heat transfer in the high Arctic.

7.4.4.5. Midwinter image of the Chukchi Sea. Figure 7-20(d) shows three altimeter tracks overlaid on an AVHRR channel 4 image of the Chukchi Sea acquired on March 14, 1988. All three tracks show numerous peaks in the echo strength, especially near coasts and islands. Here, leads are most likely to occur when winds blow older ice away from the coast, allowing new ice to form. Judging by high *SIGPK* and *SIGTD* values, a large area of new ice may be north of Wrangel Island, although this is difficult to observe in the imagery. This again shows the usefulness of altimetry as an adjunct to visible or infrared imagery.

7.4.4.6. Altimetry coincident with passive microwave imagery. Satellite passive microwave data has been widely used for mapping global sea ice cover. Satellite altimetry provides the only practical alternative means for global synoptic monitoring of sea ice extent. The merging and comparison of data from these two sensors is therefore an obvious means to improve understanding of both [Laxon and Askne, 1991].

In the following analysis we examine data from a merged product produced using data from the Geosat altimeter and the SSM/I flown on board the Defense Meteorological Satellite Program (DMSP) satellite series. The five brightness

temperatures recorded by the SSM/I for the day and location of each altimeter data point are appended to the Geosat Geophysical Data Record (GDR). The spatial coincidence is therefore within 25 km (the gridded resolution of daily average SSM/I brightness temperatures) and the temporal coincidence within one day. The merged data set can then be used to directly compare the ice extent mapped by the two sensors. The SSM/I data are processed using the NASA Team algorithm. The algorithm used for detecting the ice edge in the Geosat data record uses the standard deviation of the 10 surface height values recorded in the GDR over 1 second. Over sea ice, the disruption of the tracker (described in Section 7.2) results in a significant increase in the standard deviation of the height measurement [Laxon, 1990]. Other algorithms have used the rise in *AGC* and the drop in *SWH* to detect the ice edge and the penetration of swell in the MIZ [Rapley, 1984] and the rise in the ratio of *AGC* to *VATT* that occurs as the edge is crossed [Hawkins and Lybanon, 1989].

Figure 7-21 shows a series of altimeter tracks for August 3, 1987 overlaid on a polarization difference image generated from the 85 GHz channel. Although the 85 GHz channel suffers from some weather contamination, the ice cover is reasonably visible. A data point is plotted in white where both sensors indicate that ice is present. Where only the altimeter indicates ice the data point is plotted in red. Where only the SSM/I indicates sea ice is present the data point is plotted in green. If neither sensor indicates that ice is present, a blue data point is plotted. Both sensors show an ocean signal in most areas away from the ice boundary, with the exception of some green points north of Scandinavia where the SSM/I incorrectly identifies some areas as being ice covered. It is well known that the SSM/I maps some areas of open water as ice due to weather effects. In the Beaufort and Chukchi Seas, various areas of both green and red points are observed. The red points appear to lie near the ice boundary, while the green points occur within the pack (in one case over what might be an area of open water). Small areas of red points are also observed in the Kara and Greenland Seas. These may delineate ice cover below the lowest concentration detectable using SSM/I.

In order to look at the Geosat altimeter and SSM/I differences on a larger scale, two 17-day merged data sets were compiled, one during midwinter and one during midsummer for both hemispheres. The data plots produced from these data sets do not show any points where both instruments indicate no ice to be present. This is to permit clearer delineation of areas of disagreements. Figure 7-22(a) shows data for August 1987 in the Northern Hemisphere. The amount of ice cover below 72° N (the northern limit of coverage) is limited, but significant clusters of red points are observed in the Greenland, Beaufort, Barents, and Kara Seas. At lower latitudes, such as around the British Isles, a large number of green data points illustrate the problem of weather effects in the SSM/I data. Figure 7-22(b) shows the corresponding image for February 1988. During maximum extent there is much better agreement overall between the altimeter and the SSM/I. The few

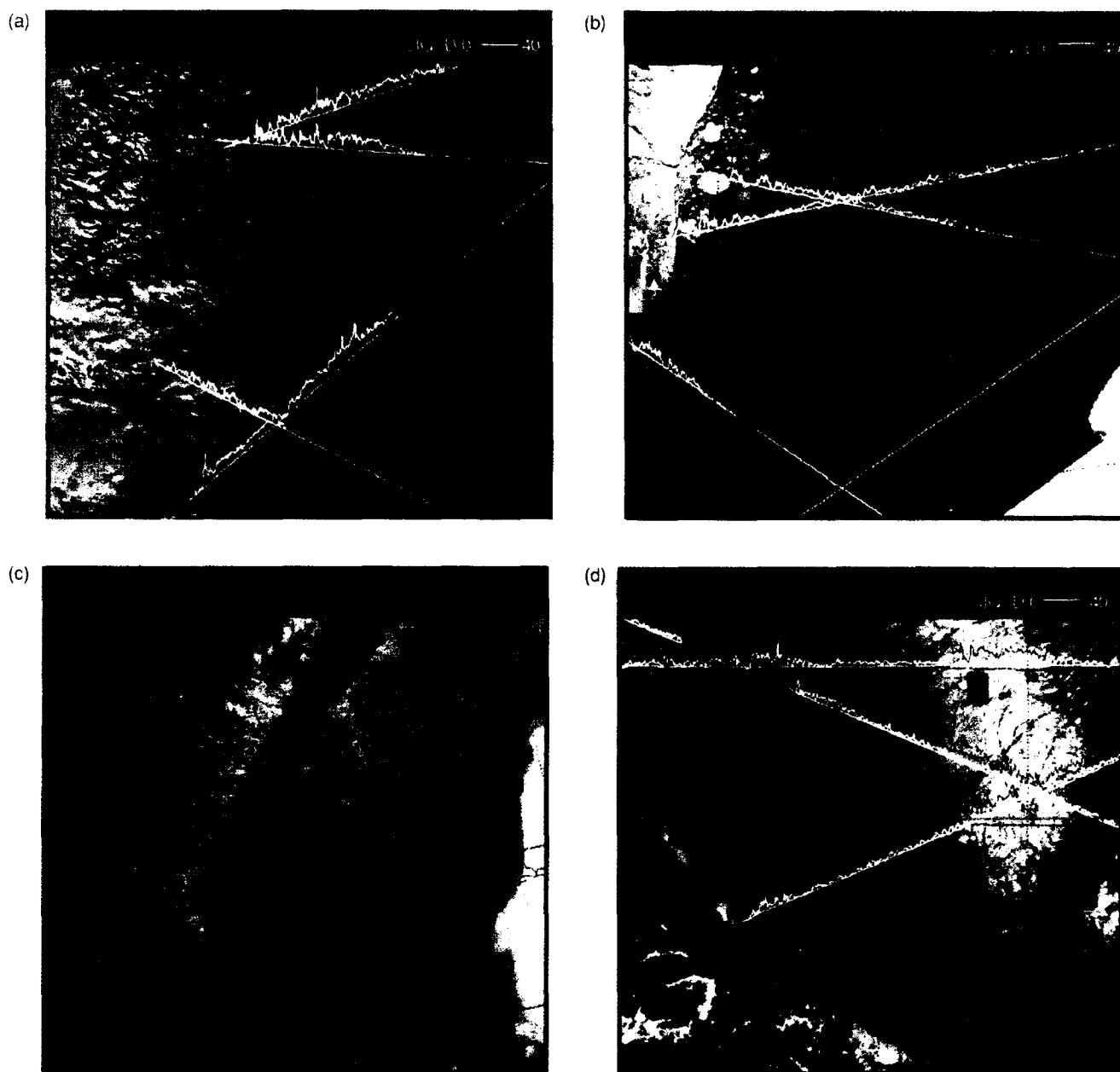


Fig. 7-20. (a) An AVHRR visible image of the Greenland Sea, with altimeter waveform parameters overlaid along the Geosat altimeter track (Scoresby Sound is near the center of the image); (b) as in (a), but with a less compact ice edge; (c) infrared band image of the Kara Sea, with Geosat AGC values plotted every 0.1 s along the nadir track; and (d) infrared band image of the Chukchi Sea, with waveform parameters.

exceptions are in the Chukchi Sea, around 165° E, and in the Greenland Sea, where some green points are observed. These points may be attributable to areas of fast ice and vast floes which, as seen in the comparisons with AVHRR data, result in an altimeter signal that is difficult to distinguish from open water.

Figure 7-22(c) shows the Southern Hemisphere during February 1988. There is a clear geographic zonation of

green and red points. Since the altimeter samples the ice edge at random points during the 17-day period, the fact that the areas of disagreement are geographically correlated strongly suggests some geophysical cause. Red points in particular are observed mainly in the Weddell and Ross Seas, with green points occurring in the Bellingshausen Sea and along the eastern coast of the Antarctic continent. The cause of this discrepancy is not understood, but the

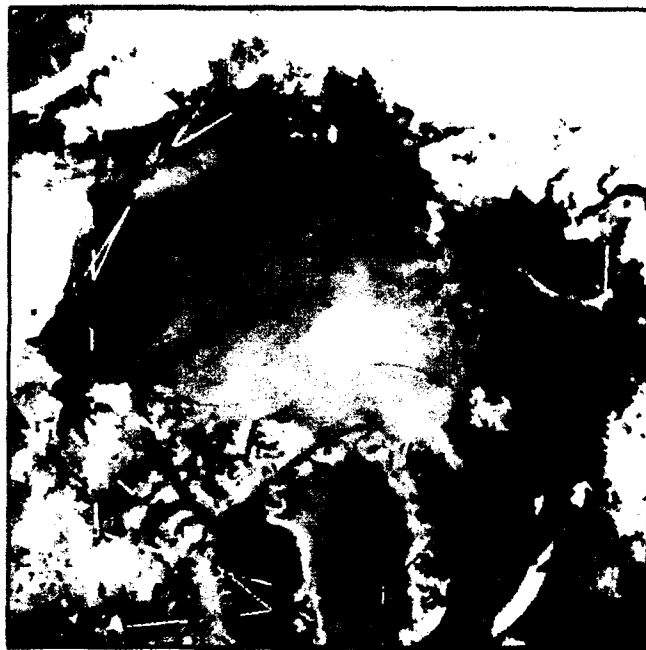


Fig. 7-21. An August 3, 1987, SSM/I 85-GHz polarization difference image.

implications for ice edge mapping are significant, since the altimeter is routinely identifying an ice edge nearly 100 km outside that identified by SSM/I in some areas. The green points on the eastern part of the continent might be attributable to fast ice, but those in the Bellingshausen Sea are more difficult to interpret. In contrast to the Northern Hemisphere weather effects do not seem to result in so many green points over the open ocean. Figure 7-22(d) shows the corresponding image for August 1987. Again there is better overall agreement during the winter period, with very few red points occurring anywhere. Some areas of green points are observed mainly in the Bellingshausen Sea. The reason for this is not fully understood. It may be attributable to areas of nearly 100% ice cover, resulting in an ocean-like altimeter signal.

7.5 SUMMARY

Potential users of radar altimetry will find sources for data from past, present, and future missions listed in Massom [1991], with a treatment of the applicability of the data to polar studies. Methods for extracting various ice parameters from the data record have been suggested in this chapter. Additional parameters and alternative ways of deriving parameters can be found in the literature (e.g., Rapley et al. [1987]).

Generally, ice parameters are arrived at by first retracking and editing the altimeter data record and then deriving waveform parameters that are linked to the desired ice parameters. The processing required to derive a waveform parameter and the strength of theory linking it to

an ice parameter vary. Ulander, for instance, calculates backscatter from waveforms and classes ice on the basis of backscatter [Ulander, 1991]. Drinkwater [1991] finds the theoretically inverse relationship between the integral of waveform power and ice concentration borne out in measurements. Chase and Holyer [1990] perform a sophisticated analysis of waveform shape, and empirically link shape to different ice types and concentrations. Other algorithms use parameters that are more distantly derived from waveform power and shape. For instance, SWH has been used to measure swell penetration of the MIZ, and AGC has been used to mark the ice edge (see Section 7.4.4). While AGC and SWH can be processed quickly and are more readily available than the waveforms themselves, they are the result of averaging waveforms and therefore have disadvantages. Yet another approach is to link variability in waveform parameters with ice conditions. Variability in waveform power aids in the delineation of zones in Figure 7-18, while the standard deviation of the height measurement is used in Section 7.4.4 to locate the ice edge.

With the exception of ice edge, it has not been demonstrated that any ice parameter can be reliably retrieved from altimetry on more than a case study basis. The research reported here strongly indicates that this will change. The best hope for progress in this direction may lie in seeking an empirical connection between waveform parameters and ice conditions using global satellite data sets.

Acknowledgments.

The work of F. M. Fetterer was supported by the Office of Naval Research under program element 0603704N, CDR P. Ranelli, Program Manager. S. W. C. Laxon's work was supported by the U.K. Science and Engineering Research Council. L. M. H. Ulander was supported by the Swedish Board of Space Activities for this study.

REFERENCES

- Beckmann, P. and A. Spizzichino, *The Scattering of Electromagnetic Waves From a Rough Surface*, 503 pp., Pergamon Press, New York, 1963.
- Brown, G. S., A theory for near-normal incidence microwave scattering from first-year sea ice, *Radio Science*, 17(1), pp. 233-243, 1982.
- Chase, J. R. and R. J. Holyer, Estimation of sea ice type and concentration by linear unmixing of Geosat altimeter waveforms, *Journal of Geophysical Research*, 95(C10), pp. 18,015-18,025, 1990.
- Chelton, D. B. and P. J. McCabe, A review of satellite altimeter measurement of sea surface wind speed: with a proposed new algorithm, *Journal of Geophysical Research*, 90, pp. 4707-4720, 1985.
- Chelton, D. B., E. J. Walsh, and J. L. MacArthur, Pulse compression and sea level tracking in satellite altimetry, *Journal of Atmospheric and Oceanic Technology*, 6, pp. 407-438, 1989.

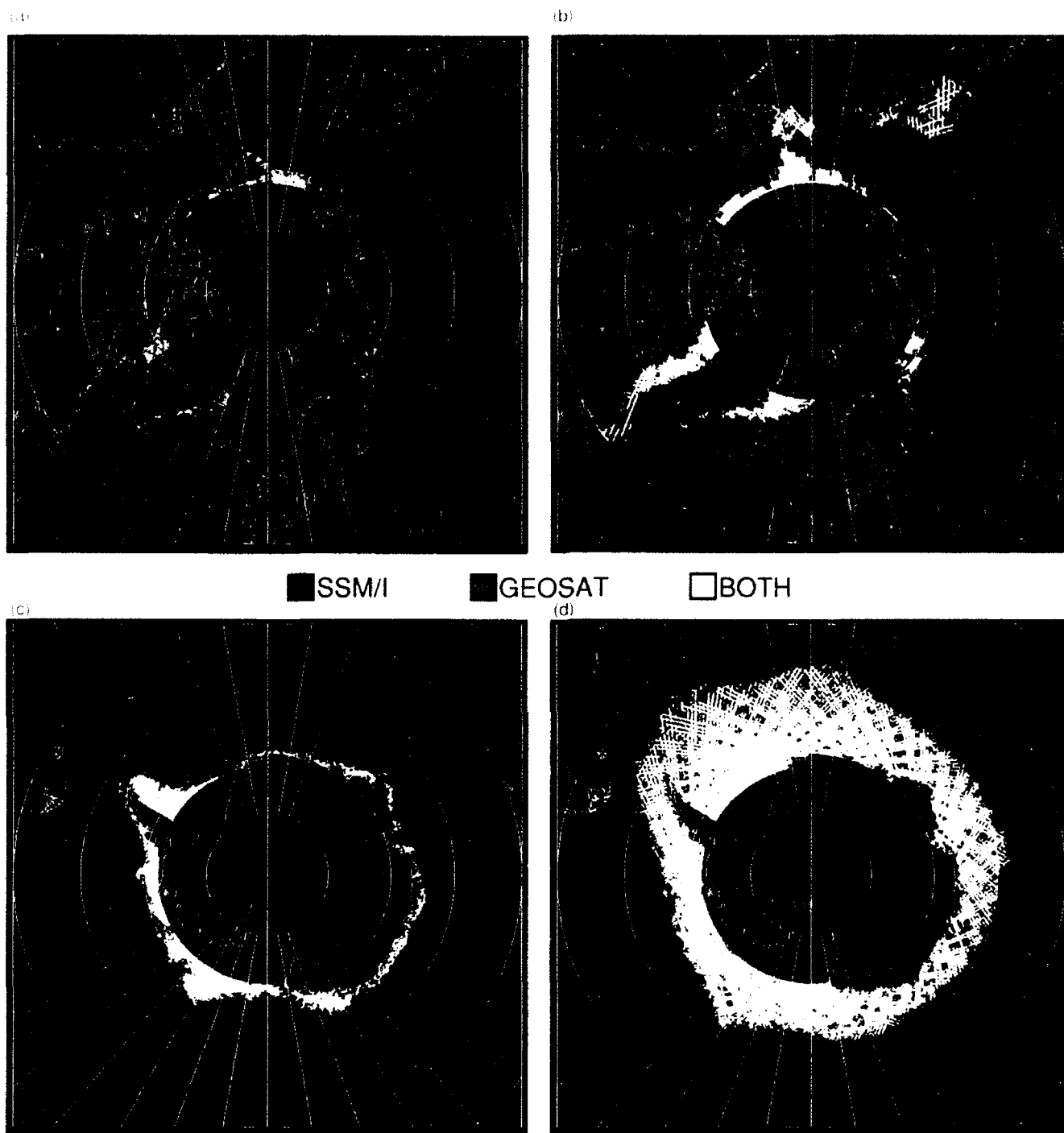


Fig. 7-22. A merged SSM/I and altimeter data product for (a) August 1987, and (b) February 1988, in the Northern Hemisphere, and (c) February 1988, and (d) August 1987, in the Southern Hemisphere. Colors indicate the detection of ice by either or both sensor.

- Chen, K. S. and A. K. Fung, A scattering model for ocean surface, *Proceedings of the International Geoscience and Remote Sensing Symposium (IGARSS'91)*, pp. 1251–1254, European Space Agency, Helsinki, Finland, 1991.
- Cowan, A. M. and V. A. Squire, *Sea Ice Characteristics Derived From Airborne Altimetry*, pp. 125–128, ESA SP-221, European Space Agency, Helsinki, Finland, 1984.
- Drinkwater, M. R., *Radar Altimetric Studies of Polar Ice*, Ph.D. dissertation, Scott Polar Research Institute, University of Cambridge, Cambridge, England, 231 pp., 1987.
- Drinkwater, M. R., Ku-band airborne radar altimeter observations of sea ice during the 1984 Marginal Ice Zone Experiment, *Journal of Geophysical Research Special MIZEX Issue*, 96(C3), pp. 4555–4572, 1991.
- Dwyer, R. E. and R. H. Godin, *Determining Sea-Ice Boundaries and Ice Roughness Using GEOS-3 Altimeter Data*, NASA Contractor Report 156862, 47 pp., National Aeronautics and Space Administration, Washington, DC, 1980.
- Eom, H. J. and W. M. Boerner, A re-examination of radar terrain backscattering at nadir, *IEEE Transactions on Geoscience and Remote Sensing*, 24(2), pp. 232–234, 1986.
- Fedor, L. S. and E. J. Walsh, Interpretation of Seasat radar altimeter returns from an overflight of ice in the Beaufort Sea, *Conference Record: Oceans'88*, pp. 1697–1703, Marine Technology Society, Baltimore, Maryland, 1988.
- Fedor, L. S., G. S. Hayne, and E. J. Walsh, Ice type classification from airborne pulse-limited radar altimeter return waveform characteristics, *Proceedings of the IGARSS'89*, pp. 1949–1952, European Space Agency, Vancouver, Canada, 1989.
- Fetterer, F. M., S. Laxon, and D. R. Johnson, A comparison of Geosat altimeter and Synthetic Aperture Radar measurements over east Greenland pack ice, *International Journal of Remote Sensing*, 12(3), pp. 569–583, 1991.
- Fung, A. K. and H. J. Eom, Coherent scattering of a spherical wave from an irregular surface, *IEEE Transactions on Antennas and Propagation*, AP-31(1), pp. 68–72, 1983.
- Fung, A. K. and G. W. Pan, A scattering model for perfectly conducting random surfaces, I. Model development, *International Journal of Remote Sensing*, 8(11), pp. 1579–1593, 1987.
- Griffiths, H. D., D. J. Wingham, P. G. Challenor, T. H. Guymmer, and M. A. Srokosz, *A Study of Mode Switching and Fast Delivery Product Algorithms for the ERS-1 Altimeter*, ESA Contract Report 6375/85/NL/BI, European Space Agency, Noordwijk, Netherlands, 1987.
- Hawkins, J. D. and M. Lybanon, Geosat altimeter sea ice mapping, *IEEE Journal of Oceanic Engineering*, 14(2), pp. 139–148, 1989.
- Hawkins, J. D., S. Laxon, and H. Phillips, Antarctic tabular iceberg multisensor mapping, *Proceedings of the IGARSS'91*, pp. 1605–1608, European Space Agency, Helsinki, Finland, 1991.
- Kim, Y. S., R. K. Moore, R. G. Onstott, and S. Gogineni, Towards identification of optimum radar parameters for sea-ice monitoring, *Journal of Glaciology* 31(109), pp. 214–219, 1985.
- Lange, M. A. and H. Eicken, The sea ice thickness distribution in the Northwestern Weddell Sea, *Journal of Geophysical Research*, 96, pp. 4821–4838, 1991.
- Laxon, S. W. C., *Satellite Radar Altimetry Over Sea Ice*, Ph.D. thesis, 246 pp., University College London, Holmbury St. Mary Dorking, Surrey, UK, 1989.
- Laxon, S., Seasonal and interannual variations in Antarctic sea ice extent as mapped by radar altimetry, *Geophysical Research Letters*, 17(10), pp. 1553–1556, 1990.
- Laxon, S. and J. Askne, Comparison of Geosat and SSM/I mapping of sea ice in the Arctic, *Proceedings of the IGARSS'91*, pp. 1593–1596, European Space Agency, Helsinki, Finland, 1991.
- Lytle, V., K. Jezek, and S. Gogineni, Radar backscatter measurement during the winter Weddell Sea gyre study, in press, *South Antarctic Journal*, 1992.
- Massom, R., *Satellite Remote Sensing of Polar Regions*, 307 pp., Belhaven Press, London, 1991.
- McIntyre, N. F. and W. Cudlip, Observation of a giant Antarctic tabular iceberg by satellite radar altimetry, *Polar Record*, 145, pp. 458–462, 1987.
- McIntyre, N. F., H. D. Griffiths, A. R. Birks, A. M. Cowan, M. R. Drinkwater, E. Novotny, R. J. Powell, V. A. Squire, L. M. H. Ulander, and C. L. Wrench, *Analysis of Altimetry Data From the Marginal Ice Zone Experiment*, ESA Contract Report 5948/84/NL/BI, 201 pp., European Space Agency, Noordwijk, Netherlands, 1986.
- Onstott, R. G., *Multifrequency Helicopter-Borne Altimeter Observations of Summer Marginal Sea Ice During MIZEX'84*, Technical Report 239500-1-T, Environmental Research Institute of Michigan, Ann Arbor, Michigan, 1991.
- Onstott, R. G., T. C. Grenfell, C. Mätzler, C. A. Luther, and E. A. Svendsen, Evolution of microwave sea ice signatures during early summer and midsummer in the marginal ice zone, *Journal of Geophysical Research*, 92(C7), pp. 6825–6835, 1987.
- Powell, R. J., A. R. Borks, C. L. Wrench, W. J. Bradford, and B. F. Maddison, *Radar Altimetry Over Sea Ice*, pp. 129–134, ESA SP-221, European Space Agency, Noordwijk, Netherlands, 1984.
- Rapley, C. G., First observations of the interaction of ocean swell with sea ice using satellite radar altimeter data, *Nature*, 307, pp. 150–152, 1984.
- Rapley, C. G., H. D. Griffiths, V. A. Squire, M. LeFebvre, A. R. Birks, A. C. Brenner, C. Brossier, L. D. Clifford, A. P. R. Cooper, A. M. Cowan, D. J. Drewry, M. R. Gorman, H. E. Huckle, P. A. Lamb, T. V. Martin, N. F. McIntyre, K. Milne, E. Novotny, G. E. Peckham, C. Schgounn, R. F. Scott, R. H. Thomas, and J. F. Vesecky, *A Study of Satellite Radar Altimeter Operation Over Ice Covered Surfaces*, 240 pp., ESA Contract Report 5182/82/F/CG(SC), European Space Agency, Noordwijk, Netherlands, 1983.

- Rapley, C. G., M. A. J. Guzkowska, W. Kudlip, and I. M. Mason, *An Exploratory Study of Inland Water and Land Altimetry Using Seasat Data*, 377 pp. ESA Contract Report CR-6483/85/NL/BI, European Space Agency, Noordwijk, Netherlands, 1987.
- Robin, G. de Q., D. J. Drewry, and V. A. Squire, Satellite observations of polar ice fields, *Philosophical Transactions of the Royal Society of London*, A309, pp. 447–461, 1983.
- Shapiro, A. and B. S. Yapple, Anomalous radar backscattering from terrain at high altitudes at nadir, *Proceedings of the IEEE*, 63(4), pp. 717, 1975.
- Swift, C. T., W. J. Campbell, D. J. Cavalieri, P. Gloersen, H. J. Zwally, L. S. Fedor, N. M. Mognard, and S. Peteherych, Observations of the polar regions from satellites using active and passive microwave techniques, *Advances in Geophysics*, 27, pp. 335–393, 1985.
- Tucker, W. B., A. J. Gow, and W. F. Weeks, Physical properties of summer sea ice in the Fram Strait, *Journal of Geophysical Research*, 92(C7), pp. 6787–6803, 1987.
- Ulaby, F. T., R. K. Moore, and A. K. Fung, *Microwave Remote Sensing—Active and Passive*, Vol. II: Radar Remote Sensing and Surface Scattering and Emission Theory, Addison-Wesley Publishing Company, Reading, Massachusetts, 1982.
- Ulander, L. M. H., Interpretation of Seasat radar-altimeter data over sea ice using near-simultaneous SAR imagery, *International Journal of Remote Sensing*, 8(11), pp. 1679–1686, 1987a.
- Ulander, L. M. H., *Seasat Radar Altimeter and Synthetic Aperture Radar: Analysis of an Overlapping Sea-Ice Data Set*, Research Report 159, Department of Radio and Space Science, Chalmers University of Technology, Göteborg, Sweden, 1987b.
- Ulander, L. M. H., Averaging radar altimeter pulse returns with the interpolation tracker, *International Journal of Remote Sensing*, 8, pp. 705–721, 1987c.
- Ulander, L. M. H., Observations of ice types in satellite altimeter data, *Proceedings of the IGARSS'86*, pp. 655–658, European Space Agency, Edinburgh, UK, 1988.
- Ulander, L. M. H., *Radar Remote Sensing of Sea Ice: Measurements and Theory*, Technical Report 212, Chalmers University of Technology, School of Electrical and Computer Engineering, Göteborg, Sweden, 1991.
- Ulander, L. M. H. and A. Carlström, Radar backscatter signatures of Baltic sea ice, *Proceedings of the IGARSS'91*, pp. 1215–1218, European Space Agency, Helsinki, Finland, 1991.
- Wadhams, P., A mechanism for the formation of ice bands, *Journal of Geophysical Research*, 88(C5), pp. 2813–2818, 1983.
- Wadhams, P., M. A. Lange, and S. F. Ackley, The ice thickness distribution across the Atlantic sector of the Antarctic Ocean in midwinter, *Journal of Geophysical Research*, 92(C13), pp. 14,535–14,552, 1987.
- Wadhams, P., V. A. Squire, D. J. Goodman, A. M. Cowan, and S. C. Moore, The attenuation rates of ocean waves in the marginal ice zone, *Journal of Geophysical Research*, 93(C6), pp. 6799–6818, 1988.
- Wingham, D. J. and C. G. Rapley, Saturation effects in the Seasat altimeter receiver, *International Journal of Remote Sensing*, 8, pp. 1163–1173, 1987.